



Calhoun: The NPS Institutional Archive
DSpace Repository

Theses and Dissertations

1. Thesis and Dissertation Collection, all items

2004-09

Naval Postgraduate School anechoic chamber evaluation

Erenoglu, Burcak

Monterey California. Naval Postgraduate School

<http://hdl.handle.net/10945/1437>

Copyright is reserved by the copyright owner.

Downloaded from NPS Archive: Calhoun



Calhoun is the Naval Postgraduate School's public access digital repository for research materials and institutional publications created by the NPS community. Calhoun is named for Professor of Mathematics Guy K. Calhoun, NPS's first appointed -- and published -- scholarly author.

Dudley Knox Library / Naval Postgraduate School
411 Dyer Road / 1 University Circle
Monterey, California USA 93943

<http://www.nps.edu/library>



NAVAL POSTGRADUATE SCHOOL

MONTEREY, CALIFORNIA

THESIS

**NAVAL POSTGRADUATE SCHOOL ANECHOIC
CHAMBER EVALUATION**

by

Burcak Erenoglu

September 2004

Thesis Advisor:
Second Reader:

David C. Jenn
Curtis Schleher

Approved for public release; distribution is unlimited

THIS PAGE INTENTIONALLY LEFT BLANK

REPORT DOCUMENTATION PAGE			<i>Form Approved OMB No. 0704-0188</i>	
Public reporting burden for this collection of information is estimated to average 1 hour per response, including the time for reviewing instruction, searching existing data sources, gathering and maintaining the data needed, and completing and reviewing the collection of information. Send comments regarding this burden estimate or any other aspect of this collection of information, including suggestions for reducing this burden, to Washington headquarters Services, Directorate for Information Operations and Reports, 1215 Jefferson Davis Highway, Suite 1204, Arlington, VA 22202-4302, and to the Office of Management and Budget, Paperwork Reduction Project (0704-0188) Washington DC 20503.				
1. AGENCY USE ONLY (Leave blank)		2. REPORT DATE September 2004	3. REPORT TYPE AND DATES COVERED Master's Thesis	
4. TITLE AND SUBTITLE: Naval Postgraduate School Anechoic Chamber Evaluation			5. FUNDING NUMBERS	
6. AUTHOR(S) Burcak Erenoglu				
7. PERFORMING ORGANIZATION NAME(S) AND ADDRESS(ES) Naval Postgraduate School Monterey, CA 93943-5000			8. PERFORMING ORGANIZATION REPORT NUMBER	
9. SPONSORING /MONITORING AGENCY NAME(S) AND ADDRESS(ES) N/A			10. SPONSORING/MONITORING AGENCY REPORT NUMBER	
11. SUPPLEMENTARY NOTES The views expressed in this thesis are those of the author and do not reflect the official policy or position of the Department of Defense or the U.S. Government.				
12a. DISTRIBUTION / AVAILABILITY STATEMENT Approved for public release, distribution is unlimited.			12b. DISTRIBUTION CODE A	
13. ABSTRACT (maximum 200 words) Antennas are designed for specific system requirements such as gain, radiation pattern, bandwidth and input impedance and patterns. During this design and testing process, one of the most important steps is the measurement of its radiation pattern to define these critical parameters. Anechoic chambers are used for indoor testing purposes. Ideally they are isolated from all kinds of electromagnetic noise and have absorber coated walls inside. They also are used for radar cross-section (RCS) measurements and electromagnetic interference tests. This thesis examines the performance of the current Naval Postgraduate School anechoic chamber. Different absorbers and antenna patterns are simulated using the Urbana Wireless Toolset. It also includes a noise evaluation of the anechoic chamber. The results of this thesis can be used to guide the users of the existing chamber configuration in setting up tests and assist in any future redesign.				
14. SUBJECT TERMS Propagation mechanisms, High frequency electromagnetic calculation techniques, Anechoic chambers, Absorber coating, Noise measurements,			15. NUMBER OF PAGES 101	
			16. PRICE CODE	
17. SECURITY CLASSIFICATION OF REPORT Unclassified	18. SECURITY CLASSIFICATION OF THIS PAGE Unclassified	19. SECURITY CLASSIFICATION OF ABSTRACT Unclassified	20. LIMITATION OF ABSTRACT UL	

THIS PAGE INTENTIONALLY LEFT BLANK

Approved for public release; distribution is unlimited

NAVAL POSTGRADUATE SCHOOL ANECHOIC CHAMBER EVALUATION

Burcak Erenoglu
Lieutenant Junior Grade, Turkish Navy
B.S, Turkish Naval Academy, 1999

Submitted in partial fulfillment of the
requirements for the degree of

MASTER OF SCIENCE IN SYSTEMS ENGINEERING

from the

**NAVAL POSTGRADUATE SCHOOL
September 2004**

Author: Burcak Erenoglu

Approved by: David C. Jenn
Thesis Advisor

Curtis Schleher
Second Reader

Dan C. Boger
Chairman, Department of Information Sciences

THIS PAGE INTENTIONALLY LEFT BLANK

ABSTRACT

Antennas are designed for specific system requirements such as gain, radiation pattern, bandwidth, input impedance, and patterns. During this design and testing process, one of the most important steps is the measurement of its radiation pattern to define these critical parameters. Anechoic chambers are used for indoor testing purposes. Ideally they are isolated from all kinds of electromagnetic noise and have absorber coated walls inside. They also are used for radar cross-section (RCS) measurements and electromagnetic interference tests.

This thesis examines the performance of the current Naval Postgraduate School anechoic chamber. Different absorbers and antenna patterns are simulated using the Urbana Wireless Toolset. It also includes a noise evaluation of the anechoic chamber. The results of this thesis can be used to guide the users of the existing chamber configuration in setting up tests and assist in any future redesign.

THIS PAGE INTENTIONALLY LEFT BLANK

TABLE OF CONTENTS

I.	INTRODUCTION.....	1
A.	BACKGROUND	1
B.	OBJECTIVES	3
C.	ORGANIZATION OF THESIS	3
II.	PROPAGATION FUNDAMENTALS AND THE URBANA WIRELESS TOOLSET	5
A.	PROPAGATION FUNDAMENTALS.....	5
1.	Reflection and Geometrical Optics.....	5
2.	Diffraction and the Geometrical Theory of Diffraction	8
3.	Diffuse Scattering.....	11
4.	Absorption and Small Particle Scattering	12
B.	THE URBANA WIRELESS TOOLSET	12
C.	SUMMARY	15
III.	RADAR ABSORBING MATERIALS AND ANECHOIC CHAMBERS	17
A.	INTRODUCTION.....	17
B.	DIELECTRIC AND MAGNETIC PROPERTIES OF MATERIALS.....	17
C.	THEOREMS FOR ABSORBERS.....	19
D.	DIELECTRIC MULTILAYER ABSORBERS	20
1.	Salisbury Screen.....	20
2.	Dallenbach Layer	21
3.	Multilayer Dielectric Absorbers	22
a.	<i>Jaumann Absorbers</i>	<i>23</i>
b.	<i>Graded dielectric and geometric absorbers.....</i>	<i>24</i>
E.	MAGNETIC MATERIALS.....	26
F.	ANECHOIC CHAMBERS	27
G.	SUMMARY	31
IV.	URBANA SIMULATIONS.....	33
A.	INPUT DATA FOR THE SIMULATIONS	33
1.	Geometrical model.....	33
2.	Antenna Pattern File.....	34
3.	Absorber Selection.....	35
B.	INPUT FILE GENERATION AND DISPLAYING THE RESULTS.....	36
C.	SIMULATIONS OF THE EMPTY CHAMBER.....	38
1.	Initial Urbana Simulations.....	38
2.	Absorber Coated Walls	39
D.	ESTIMATION OF THE QUIET ZONE	47
E.	SIMULATIONS WITH OBJECTS IN THE CHAMBER.....	50
1.	Perfect Electric Conductor (PEC) Plate in the chamber	50
2.	Receiver Antenna in the chamber	58
F.	SUMMARY	59

V.	SUMMARY AND CONCLUSIONS	61
A.	SUMMARY	61
B.	CONCLUSIONS	61
C.	FUTURE WORK	62
	APPENDIX.....	63
A.	URBANA INPUT FILE.....	63
B.	ANECHOIC CHAMBER MEASUREMENTS	71
C.	MATLAB CODES	77
	LIST OF REFERENCES.....	81
	INITIAL DISTRIBUTION LIST	83

LIST OF FIGURES

Figure 1.	Test facility for aircraft (From Ref. [1]).	1
Figure 2.	Sources of measurement errors for a compact range type of anechoic chamber. (From Ref [2]).	2
Figure 3.	Automotive electromagnetic compatibility testing (From Ref. [1]).	3
Figure 4.	Basic propagation mechanisms. (From Ref. [3].)	5
Figure 5.	Incident wave on a surface separating free space and dielectric media. (After Ref. [3].)	6
Figure 6.	Reflection of a ray tube at a planar interface. (After Ref. [2].)	8
Figure 7.	Diffacted ray geometry and the Keller cone. (From Ref. [2].)	9
Figure 8.	Ray-fixed coordinate system. (From Ref. [2].)	10
Figure 9.	Singly and doubly diffracted rays. (From Ref. [2].)	11
Figure 10.	Diffuse scattering. (From Ref. [6].)	11
Figure 11.	Urbana flow diagram (From Ref. [3].)	14
Figure 12.	Salisbury screen. (From Ref. [2])	21
Figure 13.	Dallenbach layer. (From Ref. [2].)	22
Figure 14.	Dallenbach layer performance. (From Ref. [2].)	22
Figure 15.	The predicted performance of Jaumann multilayer absorbers (From Ref. [10].)	23
Figure 16.	Pyramidal absorber (From Ref. [10].)	24
Figure 17.	Schematic illustration of the frequency behavior of ferrites. (After Ref. [10].)	27
Figure 18.	Specification of the anechoic chamber at the Naval Postgraduate School, Monterey, CA (Spanagel Hall Room 604)	30
Figure 19.	The noise measurement in 0-100 MHz frequency range for the Naval Postgraduate School anechoic chamber	31
Figure 20.	Naval Postgraduate School anechoic chamber facet model	33
Figure 21.	Uniform circular aperture antenna pattern for 15 degree HPBW, normalized by directivity ($a = 0.243\text{m} / D = 21.75\text{ dB}$)	35
Figure 22.	Reflectivity curve of the designed absorbers	36
Figure 23.	Vertically polarized 15 degree HPBW circular aperture with perfect absorber wall coating ($z = 58\text{ inches}$).	38
Figure 24.	Horizontally polarized 15 degree HPBW circular aperture with perfect absorber wall coating ($z = 58\text{ inches}$)	39
Figure 25.	Vertically polarized 15 degree HPBW antenna with -8.3 dB absorber wall coating, total field.	40
Figure 26.	Horizontally polarized 15 degree HPBW antenna with -8.3 dB absorber wall coating, total field.	40
Figure 27.	Vertically polarized 15 degree HPBW antenna with -8.3 dB absorber wall coating, reflections only.	41
Figure 28.	Horizontally polarized 15 degree HPBW antenna with -8.3 dB absorber wall coating, reflections only	41

Figure 29.	Vertically polarized 20 degree HPBW antenna with -8.3 dB absorber wall coating, total field.	42
Figure 30.	Horizontally polarized 20 degree HPBW antenna with -8.3 dB absorber wall coating, total field.	42
Figure 31.	Vertically polarized 20 degree HPBW antenna with -8.3 dB absorber wall coating, reflections only.....	43
Figure 32.	Horizontally polarized 20 degree HPBW antenna with -8.3 dB absorber wall coating, reflections only.....	43
Figure 33.	Vertically polarized 15 degree HPBW antenna with -27 dB absorber wall coating, total field.	44
Figure 34.	Horizontally polarized 15 degree HPBW antenna with -27 dB absorber wall coating, total field.	44
Figure 35.	Vertically polarized 15 degree HPBW antenna with -27 dB absorber wall coating, reflections only.....	45
Figure 36.	Horizontally polarized 15 degree HPBW antenna with -27 dB absorber wall coating, reflections only.....	45
Figure 37.	Vertically polarized 20 degree HPBW antenna with -27 dB absorber wall coating, total field.	46
Figure 38.	Horizontally polarized 20 degree HPBW antenna with -27 dB absorber wall coating, total field.	46
Figure 39.	Vertically polarized 20 degree HPBW antenna with -27 dB absorber wall coating, reflections only.....	47
Figure 40.	Horizontally polarized 20 degree HPBW antenna with -27 dB absorber wall coating, reflections only.....	47
Figure 41.	Phase error limitation for a far-field measurement (After Ref. [2]).	48
Figure 42.	Phase error in degrees	49
Figure 43.	Amplitude error in dB.....	49
Figure 44.	Vertically polarized 15 degree HPBW antenna with -8.3 dB absorber with a PEC plate, total field.	50
Figure 45.	Vertically polarized 15 degree HPBW antenna with -8.3 dB absorber with a PEC plate and edge diffraction included, total field.	51
Figure 46.	Vertically polarized 15 degree HPBW antenna with -8.3 dB absorber, no direct contribution with a PEC plate.....	51
Figure 47.	Vertically polarized 15 degree HPBW antenna with -8.3 dB absorber, no direct contribution with a PEC plate and edge diffraction included.	52
Figure 48.	Horizontally polarized 15 degree HPBW antenna with -8.3 dB absorber with PEC plate, total field.....	52
Figure 49.	Horizontally polarized 15 degree HPBW antenna with -8.3 dB absorber with a PEC plate and edge diffraction included, total field.	53
Figure 50.	Horizontally polarized 15 degree HPBW antenna with -8.3 dB absorber, no direct contribution with a PEC plate.....	53
Figure 51.	Horizontally polarized 15 degree HPBW antenna with -8.3 dB absorber, no direct contribution with a PEC plate and edge diffraction included.	54
Figure 52.	Vertically polarized 15 degree HPBW antenna with -27 dB absorber with a PEC plate, total field.	54

Figure 53.	Vertically polarized 15 degree HPBW antenna with –27 dB absorber, no direct contribution and PEC plate with edge diffraction	55
Figure 54.	Vertically polarized 15 degree HPBW antenna with –27 dB absorber, no direct contribution with a PEC plate	55
Figure 55.	Vertically polarized 15 degree HPBW antenna with –27 dB absorber, no direct contribution with a PEC plate and edge diffraction included.	56
Figure 56.	Horizontally polarized 15 degree HPBW antenna with –27 dB absorber, with a PEC plate, total field.	56
Figure 57.	Horizontally polarized 15 degree HPBW antenna with –27 dB absorber, with a PEC plate and edge diffraction included, total field	57
Figure 58.	Horizontally polarized 15 degree HPBW antenna with –27 dB absorber, no direct contribution with a PEC plate	57
Figure 59.	Horizontally polarized 15 degree HPBW antenna with –27 dB absorber, no direct contribution with a PEC plate and edge diffraction included.	58
Figure 60.	Receiver and transmitter antenna pattern comparison	59
Figure 61.	The noise measurement in 0-100 MHz frequency range for the Naval Postgraduate School anechoic chamber	71
Figure 62.	The noise measurement in 100-200 MHz frequency range for the Naval Postgraduate School anechoic chamber	72
Figure 63.	The noise measurement in 200-300 MHz frequency range for the Naval Postgraduate School anechoic chamber	72
Figure 64.	The noise measurement in 300-400 MHz frequency range for the Naval Postgraduate School anechoic chamber	73
Figure 65.	The noise measurement in 400-500 MHz frequency range for the Naval Postgraduate School anechoic chamber	73
Figure 66.	The noise measurement in 500-600 MHz frequency range for the Naval Postgraduate School anechoic chamber	74
Figure 67.	The noise measurement in 600-700 MHz frequency range for the Naval Postgraduate School anechoic chamber	74
Figure 68.	The noise measurement in 700-800 MHz frequency range for the Naval Postgraduate School anechoic chamber	75
Figure 69.	The noise measurement in 800-900 MHz frequency range for the Naval Postgraduate School anechoic chamber	75
Figure 70.	The noise measurement in 900-1000 MHz frequency range for the Naval Postgraduate School anechoic chamber	76

THIS PAGE INTENTIONALLY LEFT BLANK

LIST OF TABLES

Table 1.	The number of sheets versus fractional bandwidth (From Ref. [9].).....	23
Table 2.	Different types of ECCOSORB materials (From Ref. [1].).....	26
Table 3.	Different types of anechoic chambers (From Ref. [11].).....	29
Table 4.	Sample Urbana Input Parameters.....	37
Table 5.	Sample f2f.x input parameters	37

THIS PAGE INTENTIONALLY LEFT BLANK

ACKNOWLEDGMENTS

I would like to thank Professor David C. Jenn for his support, guidance, patience and time very much. He always answered all my questions patiently and assisted me with any problem that I had during the preparation of this thesis.

I would like to thank to my country, Turkey and Turkish Nation who brought me up as a Navy officer and giving me this opportunity for my MS degree in Naval Postgraduate School.

I would also like to thank Professor Curtis Schleher for agreeing to be the second reader to this thesis.

THIS PAGE INTENTIONALLY LEFT BLANK

I. INTRODUCTION

A. BACKGROUND

Electromagnetic (EM) waves such as television, radio, communication signals and different kinds of electromagnetic noise surround us everywhere. Wireless systems employ antennas to transmit and receive signals. The antennas have radiation patterns specifically tailored for the system. For example, radar antennas have wide beams for search and narrow beams for tracking. Similarly FM broadcast transmitter antennas have shaped beams to provide a strong signal over the desired coverage area. On the other hand, the radio set has an antenna with a broad pattern so that stations can be received from all directions.

An important step in the design of an antenna is measurement of its radiation pattern. It is the one true way to determine the antenna parameters such as gain, half-power beamwidth, and sidelobe level. Often the antenna under test is measured as installed on the vehicle so that the measurement conditions are as close as possible to the actual operating conditions. Figure 1 shows such a measurement on an aircraft antenna. Most measurements are performed on a test range that has been designed to minimize reflections from the environment that might be construed as coming from the transmit antenna. If the test range is indoors, then ideally the walls should be perfect absorbers (i.e., no energy reflected; all is absorbed). A room lined with absorbing material is referred to as an anechoic chamber.



Figure 1. Test facility for aircraft (From Ref. [1]).

In practice the walls cannot be made perfect absorbers, and therefore, error signals corrupt the antenna pattern measurements. Figure 2 illustrates some sources of measurement error in an anechoic chamber. In this case a radar cross section measurement is depicted. For an antenna measurement the target would be replaced by the antenna under test (AUT).

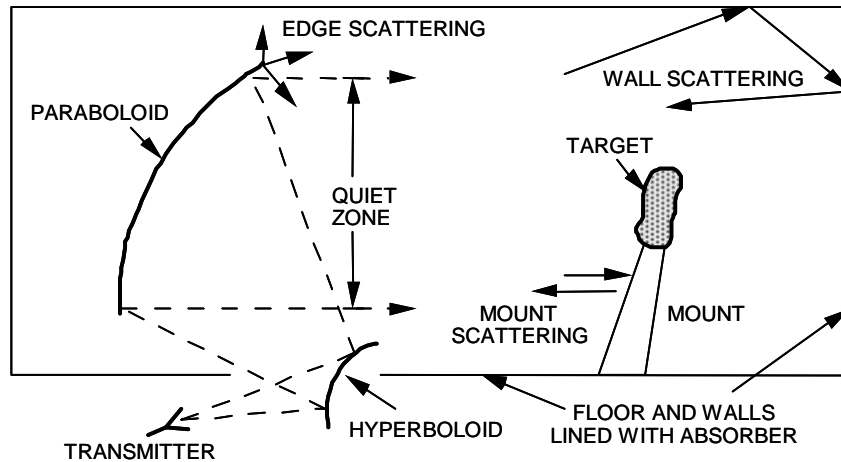


Figure 2. Sources of measurement errors for a compact range type of anechoic chamber. (From Ref [2]).

Some, but not all, anechoic chambers are designed to be electromagnetically isolated from the outside by using a shielding material between the absorber and drywall. The most effective isolation is obtained by a solid metal (conducting) plate. However, metallic screens are often used in place of a solid metal to reduce weight and cost. Isolated chambers are used to measure the electromagnetic noise generated by electronics while they are operating. For example, televisions, computers and even automobile ignition systems generate electromagnetic noise that has the potential to interfere with other electronics in the area. This is one reason why airline passengers are asked to turn off electronic equipment during take off and landing. Figure 3 shows EM emission testing being performed on an automobile in an anechoic isolation chamber.



Figure 3. Automotive electromagnetic compatibility testing (From Ref. [1]).

B. OBJECTIVES

The Naval Postgraduate School (NPS) anechoic chamber is located in Spanagel Hall, Room 604. It is used for both research and instruction; however it was built with only instruction in mind. The quality of the patterns is not as good as desired for research studies, mainly due to multiple reflections from the walls.

This thesis evaluated the anechoic chamber using both simulation and measurements. The simulations show the paths of reflection and how they change for various types of absorbers. A noise evaluation of the chamber was also performed. The results of this research will help in any future redesign of the chamber. It also serves as a guide for users of the existing chamber configuration, so that unexpected measured pattern data might be traced to the chamber characteristics.

C. ORGANIZATION OF THESIS

In Chapter II, basic propagation mechanisms and the Urbana Wireless Toolset are introduced. The three basic propagations mechanisms are: (1) reflection, (2) diffraction, and (3) scattering. These mechanisms along with geometrical optics and the geometrical theory of diffraction will be examined.

In Chapter III, the dielectric and magnetic properties of materials, and basic theory underlying radar absorbing materials are presented. In addition, anechoic

chambers, their design and properties, and the absorber types used in chambers are discussed.

In Chapter IV, the results of the anechoic chamber simulations, which are performed using the Urbana Wireless Toolset, are presented and the results are examined. Different types of absorbers and antenna beamwidths are used for these simulations.

In Chapter VI, the conclusions are summarized based on simulation results and some suggestions for future research are included.

II. PROPAGATION FUNDAMENTALS AND THE URBANA WIRELESS TOOLSET

This chapter discusses propagation fundamentals and the Urbana Wireless Toolset. It also discusses the geometrical optics (GO) ray tracing technique and the geometrical theory of diffraction (GTD) method, which are used by the Urbana Wireless Toolset for propagation modeling.

A. PROPAGATION FUNDAMENTALS

Radio wave propagation is difficult to predict for both indoor and outdoor environments. This is not due to any shortcoming in the electromagnetic theory, but rather the large numbers of scattering objects and their unpredictable locations. There are generally three basic propagation mechanisms: (1) reflection, (2) diffraction, and (3) scattering. These mechanisms are shown in the Figure 4, and discussed briefly in the following sections.

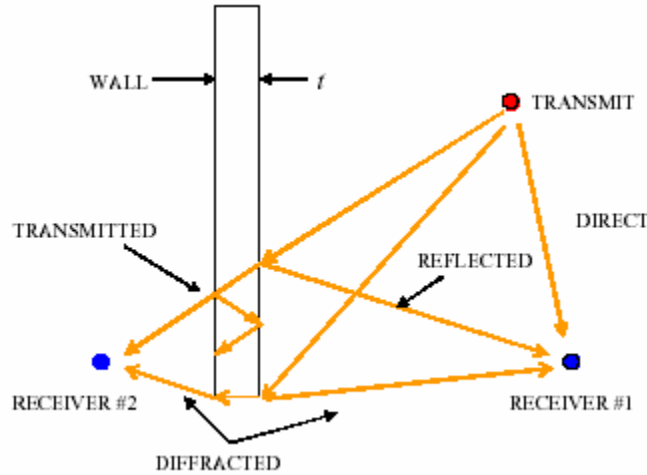


Figure 4. Basic propagation mechanisms. (From Ref. [3].)

1. Reflection and Geometrical Optics

A surface is a plane separating two media which may have different conductivity, permeability and permittivity values. It is assumed that this surface is not necessarily a perfect conductor, but is perfectly smooth and infinitely wide. If an electromagnetic wave

is incident onto this surface, some of its energy reflects back from the surface and some of its energy is transmitted into the second medium. The angle of incidence will be equal to angle of reflection by Snell's Law.

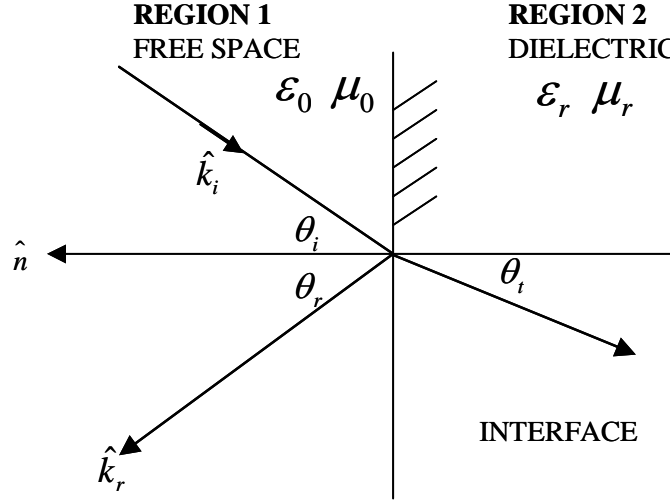


Figure 5. Incident wave on a surface separating free space and dielectric media. (After Ref. [3].)

The amplitudes of the incident wave and the reflected wave will be different. The ratio of the amplitude of the reflected wave to the incident wave is defined as *reflection coefficient*. The reflection coefficient (Γ) is dependent on polarization. For perpendicular polarization, for which the electric field vector is perpendicular to the plane defined by \hat{n} and \hat{k}_i , the reflection coefficient can be calculated from [4]

$$\Gamma_{\perp} = \frac{E_{\perp 0}^r}{E_{\perp 0}^i} = \frac{\eta_2 \cos \theta_i - \eta_1 \cos \theta_t}{\eta_2 \cos \theta_i + \eta_1 \cos \theta_t} \quad (2.1)$$

For parallel polarization, where the electric field vector is parallel to the plane defined by \hat{n} and \hat{k}_i , it can be calculated from

$$\Gamma_{\parallel} = \frac{E_{\parallel 0}^r}{E_{\parallel 0}^i} = \frac{\eta_2 \cos \theta_t - \eta_1 \cos \theta_i}{\eta_2 \cos \theta_t + \eta_1 \cos \theta_i} \quad (2.2)$$

where Γ = Fresnel reflection coefficient

E^i = Incident electric field

E^r = Reflected electric field

η = Intrinsic impedance ($\sqrt{\mu/\epsilon}$)

This smooth infinite surface approximation is accurate for most building walls, which are large compared to the wavelength.

Geometrical optics is the most basic theory that describes wave behavior upon reflection or refraction at an interface between two materials. It is also referred to as ray tracing or ray optics [2]. The electric field associated with a transverse electromagnetic wave is expressed as:

$$\vec{E} = A e^{-jks} \hat{p} \quad (2.3)$$

where $k = \frac{2\pi}{\lambda}$, λ is the wavelength, A is the complex amplitude, and s is the distance measured along a ray between the observation and reference planes. The polarization is denoted by the vector \hat{p} .

Under high frequency conditions, for a narrow radar beam illuminating a target, the radar return appears to come from specific points on target. These points can be considered as reflection points. Fields from these points can be combined for the calculation of scattering in a given direction.

The relationship between the reflected and incident fields can be obtained using the law of conservation of energy. The electric field intensity $\vec{E}(s)$ at the observation point is expressed as [5]:

$$\vec{E}(s) = \vec{E}(0) D_F e^{-jks} \Gamma \quad (2.4)$$

where $\vec{E}(0)$ is the electric field at the reflection point ($s = 0$) and Γ is the reflection coefficient. The divergence factor D_F is given by [5]:

$$D_F = \sqrt{\frac{R_1 R_2}{(R_1 + s)(R_2 + s)}} \quad (2.5)$$

where R_1 and R_2 are the principal radii of curvature of the reflected wavefront. The reflection of a tube of rays at a planar interface is shown in Figure 6.

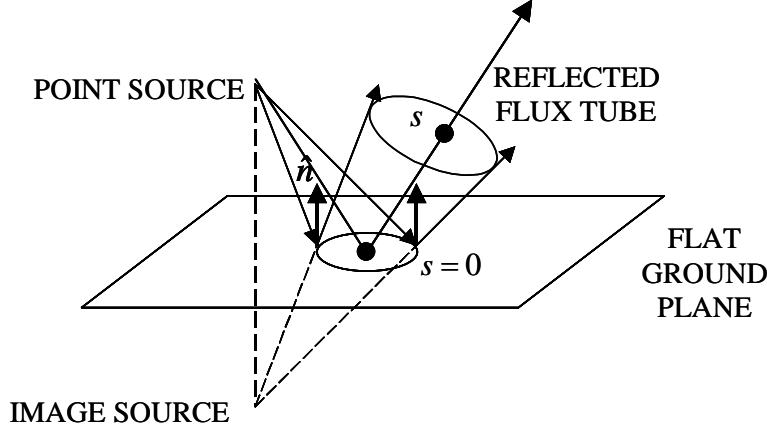


Figure 6. Reflection of a ray tube at a planar interface. (After Ref. [2].)

Formulas for the curvature of the reflected wavefront are given in Ref. [2]. Since the region of space is divided into distinct illuminated and shadow regions, geometrical optics does not take into account the edge diffraction effects.

2. Diffraction and the Geometrical Theory of Diffraction

Diffracted fields are those scattered from discontinuities such as edges and tips of an object. The waves diffracted from these objects are less intense than the reflected waves, but they can come out over a wide range of angles [2]. These edge-diffracted rays will propagate in all directions perpendicular to the edge if the incident wave is normal to the edge. For other angles, edge diffracted rays can be located anywhere along a cone with a half angle subtended by the edge and incident ray. This is known as Keller cone after J.B. Keller [2]. It is shown in Figure 7 where β'_0 and β_0 are the angles between the edge and incident scattering rays.

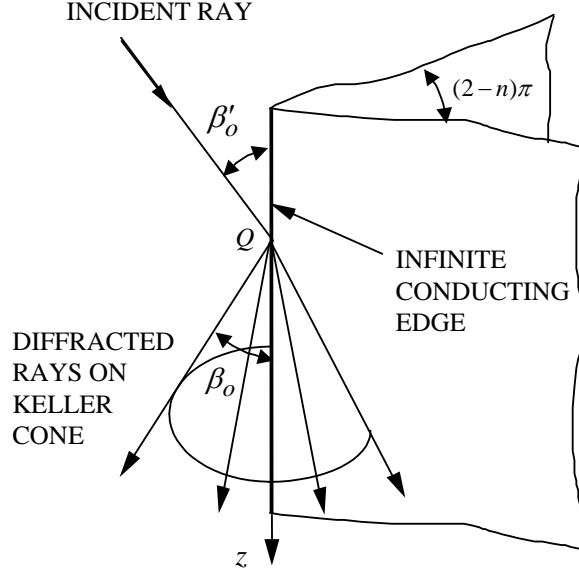


Figure 7. Diffracted ray geometry and the Keller cone. (From Ref. [2].)

The geometrical theory of diffraction (GTD) has been developed to supplement geometrical optics. It originated with Keller as an asymptotic solution of diffraction problems for high frequencies. The total field at an observation point can be divided into geometrical optics and diffracted components, and can be expressed as

$$\vec{E}_s \equiv \vec{E}_{go} + \vec{E}_{gtd} \quad (2.6)$$

The general edge diffraction geometry is shown in Figure 7. The edge is formed by the joining of two semi-infinite plates that define a wedge with internal angle $(2-n)\pi$. When $n=2$, the wedge becomes a single semi-infinite plane known as a knife edge. The diffracted waves lie on the surface of the Keller cone [2] as shown in Figure 7.

Most diffraction calculations are performed in the ray-fixed coordinate system, which is shown in Figure 8. The polarizations are defined as parallel (soft) polarization and perpendicular (hard) polarization with respect to the edge. The GTD diffracted field of the ray-fixed coordinate system can be written as

$$\vec{E}_{gtd}(P) = \left[\vec{E}_i(Q) \bullet \mathbf{D} + \frac{\partial \vec{E}_i}{\partial n} \bigg|_Q \bullet \mathbf{D}' \right] A(s, s') e^{-jks} \quad (2.7)$$

where $\vec{E}_i(Q)$ is the incident field at the diffraction point Q and $\frac{\partial \vec{E}_i}{\partial n} \bigg|_Q$ denotes the slope of the incident field at Q with respect to the normal to the edge. \mathbf{D} is a matrix of diffraction coefficients and \mathbf{D}' a matrix of slope diffraction coefficients. Formulas for these coefficients are given in Ref. [2].

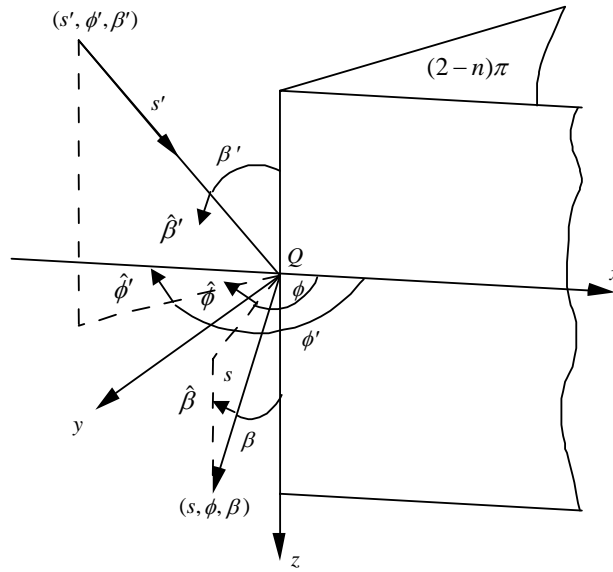


Figure 8. Ray-fixed coordinate system. (From Ref. [2].)

GO and GTD cannot be used to predict infinite fields where an infinity of rays come together, which is referred as a caustic. Defining GTD-based equivalent currents can solve the axial caustic problem. Fictitious electric and magnetic fields are considered to flow along the edges. The magnitude and phase of the currents depend on the diffraction coefficient at the edge [5]. With the GTD-based equivalent currents, edge diffracted fields remain finite in caustic directions and the scattering direction is no longer limited to a generator of the Keller cone. Formulas for the GTD-based equivalent currents are given in Ref. [2].

Double diffraction can occur between two edges as shown in Figure 9. If we consider an infinite strip, the incident wave will hit the edges and the diffracted ray will

return to the observation point. These are singly diffracted rays. One of the diffracted rays will travel along the surface and be diffracted again from the opposite edge. These are doubly diffracted rays [2]. Diffraction from test fixtures and the antenna itself can be an important contribution to the total field when an antenna is placed in the anechoic chamber.

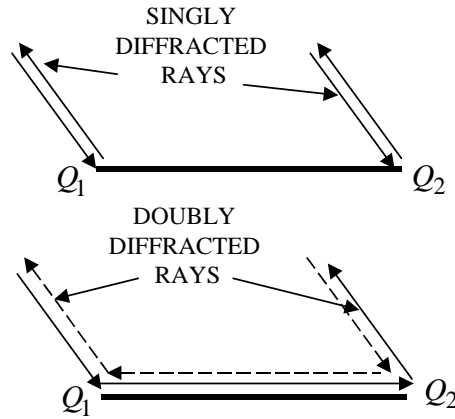


Figure 9. Singly and doubly diffracted rays. (From Ref. [2].)

3. Diffuse Scattering

Diffuse scattering is the deflection of energy in multiple directions, which is caused by a rough surface relative to the incident wavelength. Diffuse scattering randomly changes the phase and the magnitude of the wave.

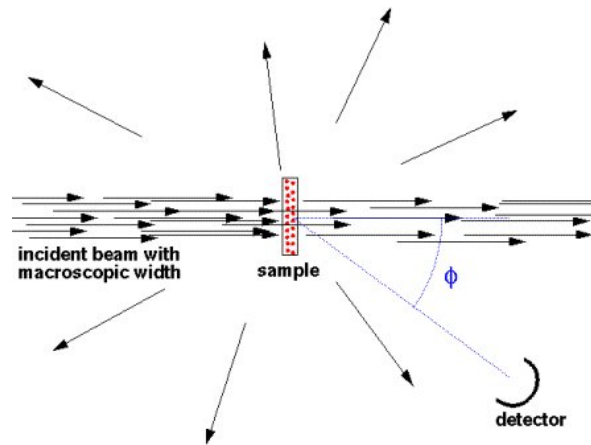


Figure 10. Diffuse scattering. (From Ref. [6].)

If the surface is not perfectly flat but its height derivates from the average less than $\lambda/16\sin\psi$ (where ψ is the incident grazing angle), then scattering effects can be ignored [7]. This is called as the Rayleigh criterion. For the smooth surface Fresnel coefficients are exact and attenuation of the signal caused by scattering is minimum. For rough surfaces Landron, Feuerstein and Rappaport [8] adjusted the Fresnel reflection coefficients by a scattering loss factor ρ_s that accounts for the energy loss caused by rough surface scattering. The scattering loss factor ρ_s can be written as

$$\rho_s = \exp \left[-8 \left(\frac{\sigma_h \pi \cos \theta_i}{\lambda} \right)^2 \right] I_0 \left[\left(\frac{\sigma_h \pi \cos \theta}{\lambda} \right)^2 \right] \quad (2.8)$$

where σ_h is the standard deviation of the surface height and I_0 is the zeroth order modified Bessel function. Many of the absorbing materials used in anechoic chambers are rough by the Rayleigh criterion. However, since only specular reflection will be of interest, the roughness can be accounted for by the loss factor in Equation (2.8).

4. Absorption and Small Particle Scattering

Absorption is a propagation mechanism by which incident energy is absorbed and converted into heat. The amount of absorption is related to the frequency of the incident wave and the dielectric properties and conductivity of the material. Absorption can also occur by small particles along the propagation path. In this case the energy is reduced by Rayleigh scattering. An example is scattering by dust particles or raindrops. Absorption and scattering are frequently defined by an attenuation coefficient.

In the design of an anechoic chamber, the wall materials are intentionally constructed to be efficient absorbers.

B. THE URBANA WIRELESS TOOLSET

Urbana is a powerful computational electromagnetic (CEM) tool for simulating wireless propagation and near field radar sensors in complex environments. The underlying ray tracing physics engine aggregates GO and GTD to produce a high-fidelity

three-dimensional simulation [9]. Urbana can be used for indoor/outdoor propagation, urban propagation and antenna simulations. In order to simulate the anechoic chamber GO and GTD ray tracing will be performed by the Urbana Wireless Toolset.

The Urbana Wireless Toolset is a UNIX based toolset comprised of the following components:

1.) **Cifer:** Generates, modifies, and translates some simple buildings and simple geometrical shapes. It is mainly used to translate building files imported from other drawing programs, and convert them into the facet file format required by Urbana.

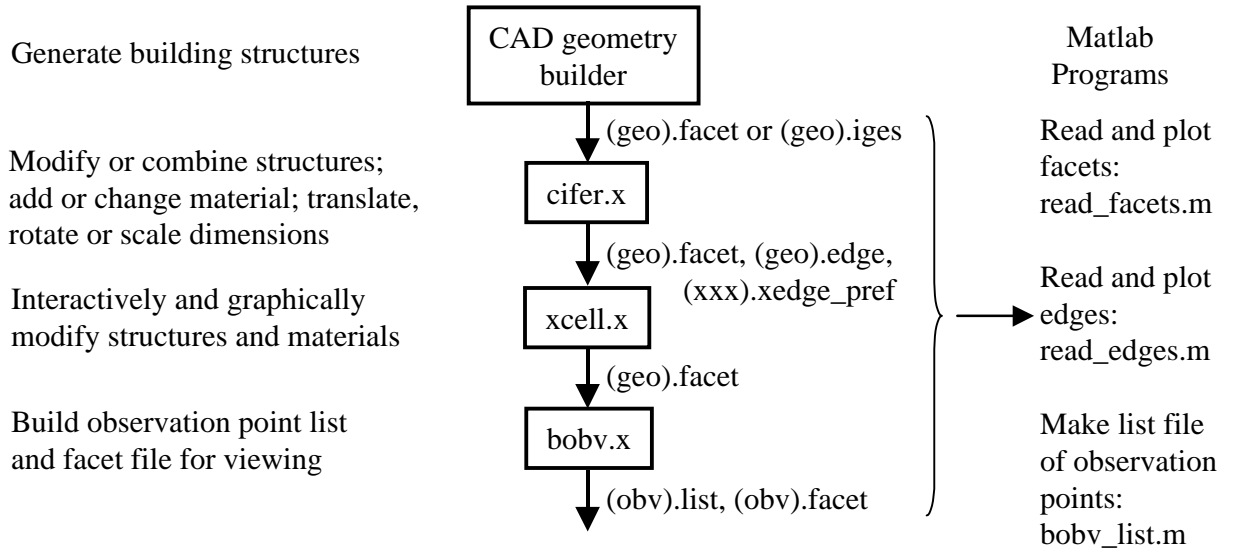
2.) **Urbana:** Determines the signal levels for the specified inputs at given observation points. There are different electromagnetic algorithms to select from, but all are based on high frequency assumptions.

3.) **Xcell:** Is used to visualize three-dimensional models of the facet files and the signal strength contours. The signal levels can be plotted as color coded cells or pixels. Xcell can also be used to delete facets and change their material properties.

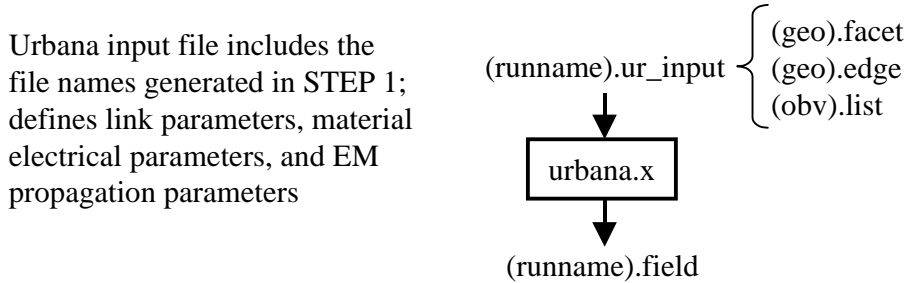
In addition to these three programs there are several auxiliary programs like f2f.x and bobv.x to format and translate data for post processing. Upon execution Urbana reads a file specified by the user that has a .ur_input extension. It is an ASCII file that is comprised of a series of code words followed by the computation parameters. A sample input file is included in the Appendix A. There are comment lines describing the parameters and their range of values. Any text editor can be used to modify the file [3].

A Silicon Graphics Inc. Octane computer with 400 MHz CPU and 1 GB memory was used for running simulations. The flowchart and the relations between these programs are shown in Figure 11.

STEP 1: GENERATING INPUT DATA FILES



STEP 2: GENERATE URBANA INPUT FILE AND RUN URBANA



STEP 3: POST PROCESSING

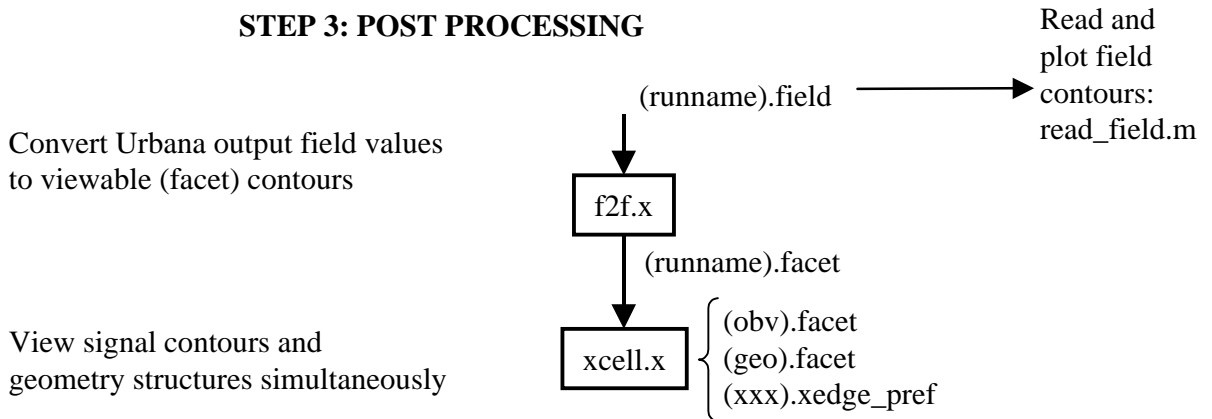


Figure 11. Urbana flow diagram (From Ref. [3].)

C. SUMMARY

This chapter presented basic propagation mechanisms, and described two of the high frequency EM techniques that will be used in the simulations: GO and GTD. The Urbana Wireless Toolset was selected for the simulation tool, and some of its capabilities were discussed.

In the next chapter anechoic chambers and radar absorbing materials (RAM) used in their walls will be discussed.

THIS PAGE INTENTIONALLY LEFT BLANK

III. RADAR ABSORBING MATERIALS AND ANECHOIC CHAMBERS

A. INTRODUCTION

Radar absorbing material (RAM) reduces the electromagnetic energy reflected from a surface through the mechanisms of absorption and cancellation. RAM has a variety of important applications such as RCS reduction of vehicles, reflectionless anechoic chamber design, and for edge loading low-sidelobe antennas. Different types RAM are widely used in anechoic chamber applications.

The RAM approach is based on finding a material that has suitable dielectric or magnetic properties for creating the right impedance to the incident wave. In addition, if the material is coating a PEC, then it is desirable to introduce as much attenuation in the RAM as possible so that the reflections from the back face are absorbed before they return to the front face. The requisite material requires the right combination of absorbing and matching properties. The absorbing material should have sufficient frequency response, and be capable of performing over the specified aspect angles as well.

This chapter represents the basic theory of RAM, some theorems for absorbers, some design approaches of RAM, and the current types of RAM structures. This chapter also includes information on anechoic chambers, different anechoic chamber designs, and the selection of RAM for chamber applications.

B. DIELECTRIC AND MAGNETIC PROPERTIES OF MATERIALS

Absorption and cancellation are the two main mechanisms for reduction of reflected energy at radar frequencies. Coatings reduce the reflected energy by the cancellation of multiple reflections. Absorption occurs by the transfer of energy from the incident wave to the material when it passes through. The absorption loss mechanisms are generally classified as ohmic, dielectric, and magnetic.

The loss properties of the material are related to its conductivity (σ), permeability (μ) and permittivity (ϵ) values. Generally the relative permittivity (ϵ_r) and relative

permeability (μ_r) are used for expressing the complex permittivity and permeability. Their complex notations are given as

$$\begin{aligned}\varepsilon &= \varepsilon' - j\varepsilon'' = \varepsilon_0(\varepsilon_r' - j\varepsilon_r'') \\ \mu &= \mu' - j\mu'' = \mu_0(\mu_r' - j\mu_r'')\end{aligned}\tag{3.1}$$

where the real (energy storage) part of the notation is denoted as a prime and the imaginary (loss) part of the notation is denoted as a double prime. The free space values are $\varepsilon_0 = 8.85 \times 10^{-12}$ F/m and $\mu_0 = 4\pi \times 10^{-7}$ H/m.

Conductivity (σ) is the main loss mechanism for the electric conductors and it can be expressed in terms of an equivalent ε_r'' . They are related by [10]

$$\varepsilon_r'' = \sigma / \omega \varepsilon_0 \tag{3.2}$$

The electric and magnetic loss tangents are expressed as

$$\begin{aligned}\tan \delta &= \varepsilon_r'' / \varepsilon_r' \\ \tan \delta_m &= \mu_r'' / \mu_r'\end{aligned}\tag{3.3}$$

Typical electric loss tangent values range between 0.001-0.1 and the resulting attenuation of the wave in decibels is small for these values. The relative permittivity (ε_r) and permeability (μ_r) can be written in terms of the loss tangent values. In polar notation they are expressed as

$$\begin{aligned}\varepsilon_r &= |\varepsilon_r| e^{j\delta_\varepsilon} \\ \mu_r &= |\mu_r| e^{j\delta_\mu}\end{aligned}\tag{3.4}$$

The intrinsic impedance (η) is defined as the impedance seen by a plane wave propagating through the material, and it can be expressed as

$$\eta = \eta_0 \sqrt{\frac{\mu_r}{\varepsilon_r}} \tag{3.5}$$

where η_0 is the free space impedance, which is approximately equal to 377Ω .

C. THEOREMS FOR ABSORBERS

There are two common theorems for absorber coated bodies for the incident plane wave case.

The first theorem states that if a target has equal values for relative permittivity and permeability, that is $\varepsilon / \varepsilon_0 = \mu / \mu_0$ at each point, then the back scattered field is zero, provided that the incidence direction is parallel to axis of the body about which a rotation of 90 degree leaves the shape of the body, together with its material medium invariant.

The second theorem states that if a plane wave is incident on a body composed of material, the backscattered fields will be zero if the shape of the target is invariant with respect to 90-degree rotation around the direction incidence, and if $\eta_s = \eta_0$, where η_s is the surface impedance. The following impedance boundary condition must also be satisfied on the surface of the body:

$$\vec{E} - (\hat{n} \cdot \vec{E})\hat{n} = \eta_s (\hat{n} \times \vec{H}) \quad (3.6)$$

where \hat{n} is the unit outward normal to the surface and \vec{E} and \vec{H} are the electric and magnetic fields of the incident plane wave [5]. The surface impedance on S is defined as

$$\eta_s = \frac{E_{\tan}}{H_{\tan}} \quad (3.7)$$

These theorems are derived directly from the Maxwell's equations and the boundary conditions, and these apply to any frequency and include all possible scattering and loss mechanisms. Unfortunately, practical radar targets do not satisfy the geometry limitations imposed by the theorems. However, the condition that $\mu_r = \varepsilon_r$ does shed some insight into the reduction problem. Because the impedance of a medium relative free space is essentially determined by $\sqrt{\mu_r / \varepsilon_r}$, equal permeability and permittivity at every point in the material yields an impedance in the medium of η_0 . Consequently, the

reflection coefficient between the free space and the medium is zero. Note that this applies only to the specular field. Diffractions from the edges and surface waves could still yield a nonzero scattered field for a finite interface. The nonspecular contributions to scattering will be zero only if the above- mentioned geometrical conditions are satisfied [2]. Rarely are the conditions met in the real world so that these theorems can be applied directly. However, they do give insight into the requirements for matching material layers.

D. DIELECTRIC MULTILAYER ABSORBERS

Radar absorbing material is generally applied over a metal or composite structure. The objective of RAM design is to have as minimum a reflection as possible, in addition to being thin, light, long lasting, low cost and have wide frequency bandwidth. The following sections represent the commonly used RAM types, their design techniques and typical performance.

1. Salisbury Screen

The Salisbury screen shown in Figure 12 is created by placing a resistive sheet over the target surface to terminate the reflections. For this case a transmission line analysis can be performed to find the effective input impedance at the front face of the layer. The transmission line equivalent circuit is also shown in Figure 12. If the resistive film is $\lambda/4$ from the conductor, then a quarter-wavelength transmission line section transforms the short circuit into an open circuit at the conductor plate. This case can be written as

$$\frac{1}{Z_{in}} = \frac{1}{R_s} + \frac{1}{\infty} = \frac{1}{R_s} \quad (3.8)$$

To obtain zero reflectivity at normal incidence the Salisbury screen resistivity R_s should be equal to 377Ω and the spacing should be equal to $\lambda/4$. For different incidence angles, resistivity, or spacing values, there will not be complete cancellation. For a finite screen size the cancellation will not be complete, even for ideal materials, because edge diffractions from the screen and ground plane exist and do not cancel [2].

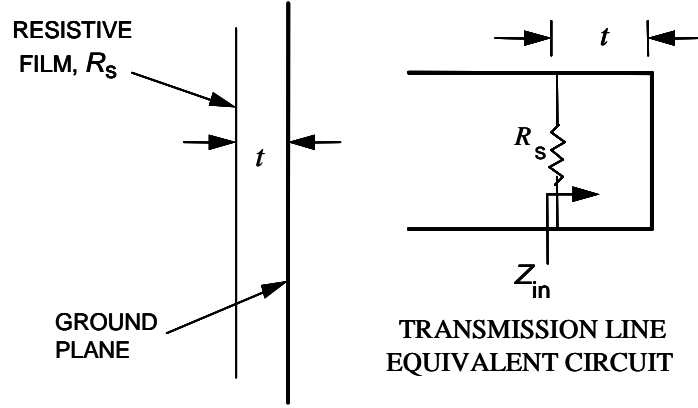


Figure 12. Salisbury screen. (From Ref. [2])

2. Dallenbach Layer

The Dallenbach layer shown in Figure 13 is a homogenous lossy layer backed by a metallic plate. The reflection from the outer surface cancels the reflection from the back surface which is achieved by choosing the right material and thickness. The reflection coefficient for the Dallenbach layer at the outer surface for normal incidence is

$$\Gamma = \frac{Z_{in} - Z_o}{Z_{in} + Z_o} \quad (3.9)$$

where

$$Z_{in} = Z_1 \frac{Z_{LOAD} + jZ_1 \tanh(\gamma t)}{Z_1 + jZ_{LOAD} \tanh(\gamma t)} \quad (3.10)$$

and Z_1 is the impedance of the layer material, Z_{LOAD} is the impedance of the back material, t is thickness of the outer surface and the complex propagation constant is $\gamma = j\omega\sqrt{\mu\epsilon}$. If the backing material is PEC then $Z_{LOAD} = 0$ and $Z_{in} = Z_d \tanh(\gamma t)$.

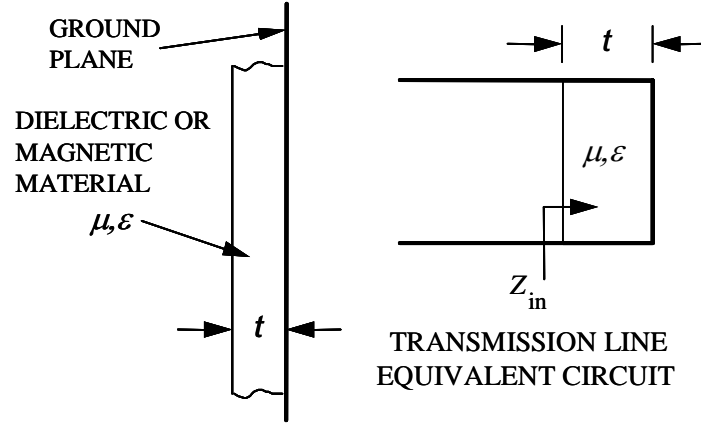


Figure 13. Dallenbach layer. (From Ref. [2].)

An example of Dallenbach layer performance for different values of permittivity and permeability is shown in Figure 14. The first drop off occurs at $0.25\lambda_0$ for electric materials and at $0.5\lambda_0$ for magnetic materials where λ_0 is the free space wavelength.

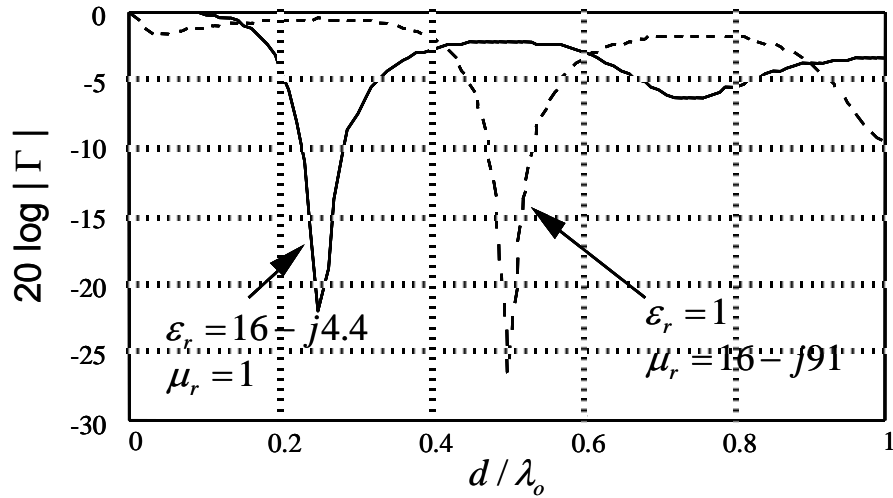


Figure 14. Dallenbach layer performance. (From Ref. [2].)

3. Multilayer Dielectric Absorbers

Single layer absorber materials usually work for limited bandwidth. In order to obtain a wide range of frequencies, multilayer absorbers are used. The multilayer dielectric absorber approach is based on slowly changing the effective impedance with distance into the material to minimize reflections. There are two common types of

multilayer dielectric absorbers: (1) Jaumann absorbers, and (2) graded dielectric and geometric absorbers.

a. Jaumann Absorbers

Jaumann absorbers are made from several Salisbury screens by combining several sheets and spacers. For maximum performance, the highest resistive sheet is located at the front.

The bandwidth of Jaumann absorbers is dependent on the number of sheets used, as illustrated in Figure 15 and Table 1. For this situation, the spacing between sheets was fixed at 7.5 mm, which is a quarter wavelength for 10 GHz, and a quadratic resistance taper was used [10].

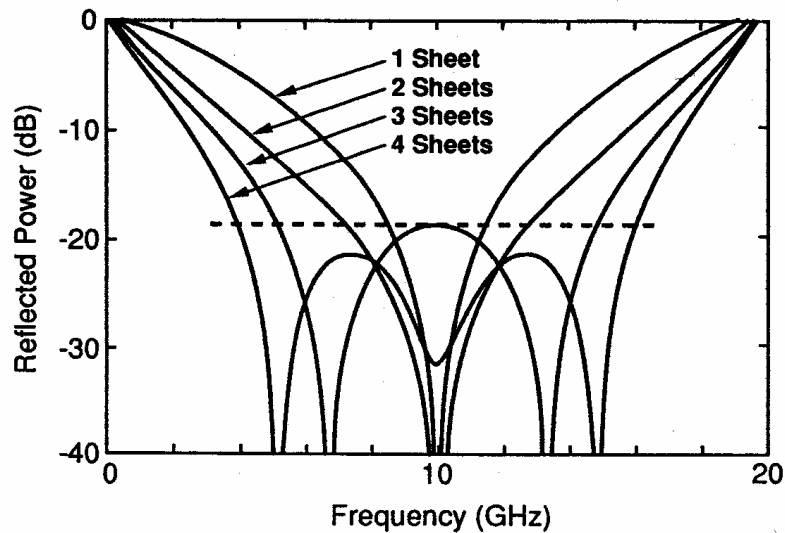


Figure 15. The predicted performance of Jaumann multilayer absorbers (From Ref. [10].)

Bandwidth of Jaumann Absorbers		
Number of sheets	Fractional Bandwidth	Total Thickness (cm)
1	0.27	0.75
2	0.55	1.50
3	0.95	2.25
4	1.16	3.00

Table 1. The number of sheets versus fractional bandwidth (From Ref. [10].)

b. Graded Dielectric and Geometric Absorbers

The graded dielectric absorbers are typically formed of discrete layers with different properties for each layer. A technique for reducing the reflection from the front face of a flat absorber is to produce a material whose intrinsic impedance is very close to unity. Two common examples are the hair-type and the carbon-loaded low-density foam absorbers. There is also a single layer graded dielectric absorber design that depends on carbon foam to provide loss, but also uses a geometric transition from free space to the highly lossy medium to provide dielectric gradient and thereby reduce reflections. This is the absorber type used in anechoic chambers. The most common one is pyramidal absorbers (Figure 16). The serrated edges of the pyramidal absorber cause dispersion of the incident plane wave by causing reflections and diffractions in all directions, thereby reducing the RCS in the transverse plane. This type of absorber can provide reflectivity reductions in excess of 50 dB, but may require thicknesses in excess of 10λ to do so [10].

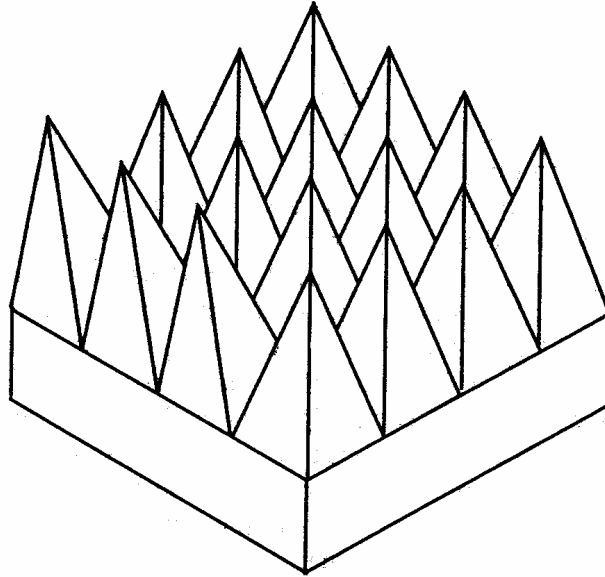


Figure 16. Pyramidal absorber (From Ref. [10].)

Achieving the impedance gradient by geometrical shaping of a medium of constant impedance provides the opportunity for a much more complete transition to take place from free space to the dissipative medium. Geometrical shaping means breaking the

front surface into an aggregate of shaped pointed elements such as cones or pyramids, where the axis of individual elements is oriented perpendicular to the plane of the absorber. A wave entering such a medium encounters a smoothly changing ratio of medium to the adjacent free space. This is similar to the case where the actual properties are changing smoothly. Where these elements are sharp, any interface reflection is negligible and only a reflection remains that is directly related to the gradient or impedance change per wavelength of depth into the medium. Such alteration of the incident surface, however, requires large physical space. Therefore, pyramidal absorbers are utilized mainly in anechoic chambers.

There are many different companies that produce absorbers for anechoic chambers. As an example, Emerson and Cuming Microwave Products provide ECCOSORB geometric absorbers. ECCOSORB is used in a wide variety of applications that span the frequency range from 30 MHz through 100 GHz. There are many different applications of ECCOSORB, such as anechoic chambers, in order to achieve free space conditions for measurement of components and systems. Several types of ECCOSORB absorbers are shown in Table 2 and more information is available in Ref. [1].

Pyramidal Absorbers

ECCOSORB® VHP-NRL	Solid, pyramidal absorber for anechoic chambers	120 MHz to 50 GHz
ECCOSORB® VFX-36-NRL	Solid, sharp-tip pyramidal absorber for microwave antenna or RCS Test ranges	± 4 dB volumetric NSA from 80 MHz
ECCOSORB® VX-20	Solid, flat-tip pyramidal absorber for compact anechoic chambers and pre-compliance emission testing	Per MIL-STD-462D
ECCOSORB® HX	Hollow, reinforced flat-tip pyramidal absorber for large shielded EMC/EMI test chambers	30 MHz to 1 GHz
ECCOSORB® VHY	Solid hybrid pyramidal absorber for small EMC test chambers	30 MHz to 30 GHz

Miscellaneous Anechoic Materials

ECCOSORB® FS	Solid, flat sheet absorber for use as free-standing absorber blocks in shielded enclosures	Above 3 GHz
ECCOSORB® FT	Sintered ferrite absorber tiles	10-1000 MHz
ECCOSORB® CV	Broadband convoluted foam microwave absorber	3 GHz to mm wave
ECCOSTOCK® ADHESIVE 13111	One part CFC-free sprayable glue for absorber to substrate adhesion	

Table 2. Different types of ECCOSORB materials (From Ref. [1].)

E. MAGNETIC MATERIALS

Characteristics of magnetic materials are determined by the permeability and magnetic loss tangent. Magnetic materials have some advantages over dielectric materials. In context of performance there is not a big difference between dielectric materials and magnetic materials, but magnetic materials generally require one-tenth of the thickness of dielectric materials to obtain the same reflection coefficient. Magnetic

RAMs are found in a number of forms and ferrite materials are commonly used for formation of the magnetic RAM. Figure 17 illustrates the frequency behavior of ferrites. It can be seen that the loss of energy increases at low frequencies with the increasing μ_r , on the other hand ϵ_r changes linearly with the increasing frequency. Magnetic materials are generally not used for chamber applications. Weight and size are not the dominant selection criteria for a chamber as they are for RCS applications on mobile platforms. However, magnetic RAM might be used in the construction of low RCS test fixtures and mounting platforms.

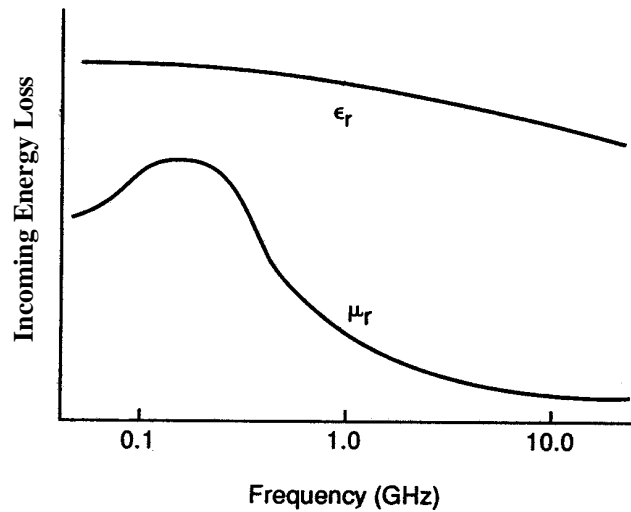


Figure 17. Schematic illustration of the frequency behavior of ferrites. (After Ref. [10].)

F. ANECHOIC CHAMBERS

Anechoic chambers are widely used for testing electromagnetic and acoustic properties all kinds of equipment. In most cases, an open environment is not appropriate for these tests because of the exposure to different noise sources that cannot be controlled. In order to have good measurements, an anechoic chamber is needed so that all unwanted signals are kept outside of the room. An anechoic chamber is an electromagnetic environment inside of which equipment can be tested and measured with a very high degree of accuracy. However, not all anechoic chambers are shielded from the outside noise environment. Chambers used for antenna pattern measurements can overcome outside noise by increasing the transmitter power. Antenna chamber designers

are more concerned with reducing reflections so that an outdoor free space propagation environment can be duplicated.

To make an anechoic chamber suitable for antenna testing, absorbers are mounted on the walls, floors, and the ceiling. The absorbers convert electromagnetic energy into heat and thus reduce undesirable reflections. If the absorbers are ideal, the surfaces become RF-invisible and these parts of the shielded room do not influence the measurement. As absorbers are not ideal materials, there may be only a small area of the room suitable for testing. This area is commonly referred to as the chamber's "quiet zone." In this area the noise levels are below the required threshold, and the incident field is planar (constant amplitude and linear phase). Restrictions might include [11]:

- At a given distance from the antenna (like 3, 5 and 10 meters) to achieve a far field condition.
- In a radius centered on the turntable to define a typical area on the turntable
- Between two heights on the turntable radius to define a volume on the turntable
- With a site attenuation deviation within limits of ± 4 dB.

Anechoic chambers can be used for measuring antenna patterns and gain, radar cross section, acoustic properties of equipments and many different applications. Anechoic chambers are usually made to meet specific requirements for a particular purpose. All features of the construction are vital for the overall performance of the chamber, and require special care during design, construction, transport, operation and maintenance. The most common anechoic chamber properties and costs are shown in Table 3 [12].

Anechoic Chamber Sizes				
Type	Size L x W x H (m)	Standards	Tests	Est. Cost* (US \$)
Smallest practical size (26MHz – 1000MHz)	7 x 3 x 3	IEC 61000-4-3	RF immunity, emission prescans and free space emissions measurements	100,000
Small (26MHz – 18 GHz)	8 x 4 x 4	IEC 61000-4-3, GR-1089 immunity	RF immunity, emission prescans and free space emissions measurements	120,000
3 meter OATS replica (26MHz – 18 GHz)	9 x 6 x 5.5	IEC 61000-4-3, ANSI C63.4, GR-1089, EN 50147-2	RF immunity and emission testing. Floor standing products up to 2 meters in dimension	285,000
5 meter OATS experimental replica (26MHz – 18 GHz)	11 x 7 x 5.5	Experimental, can be qualified as a 3 meter chamber	RF immunity and emission testing. Large floor standing products.	365,000
10 meter OATS replica (26MHz – 18 GHz)	18 x 13 x 8	IEC 61000-4-3, ANSI C63.4, GR-1089, EN 50147-2	RF immunity and emission testing. Large floor standing products.	1,100,000

Table 3. Different types of anechoic chambers (From Ref. [12].)

There are many different types of anechoic chambers, that can be used for specific frequency ranges and purposes. In this thesis, the anechoic chamber environment at the Naval Postgraduate School (NPS) is simulated by using Urbana. Different types of absorbers and antenna beamwidths are considered. The chamber is shown in Figure 18 and all dimensions are in inches. The NPS anechoic chamber was not designed for low noise emission measurements. Its primary use is antenna pattern measurements for instructional purposes. The existing chamber has only a thin foil layer between it and the wall, and there are regions where there is no foil at all. In an effort to characterize the noise levels in the chamber, on March 31, 2004 noise measurements were taken for the frequency ranges of 0-1000 MHz by Naval Postgraduate School laboratory staff. A HP-8566B spectrum analyzer and a CTS011 active broadband dipole antenna were used for

taking the measurements. The antenna works in the frequency range of 30 MHz – 2 GHz and the spectrum analyzer works in the bands from 100 Hz-2.5 GHz and 2-22 GHz. A step size of 100 MHz is used and ten measurements were taken. The first measurement result is shown in Figure 19. It is taken between 0-100 MHz and the FM band noise can be seen clearly the figure. The other frequency band measurement results can be found in the Appendix B. The final conclusion is that the NPS chamber provides little isolation from external signal sources.

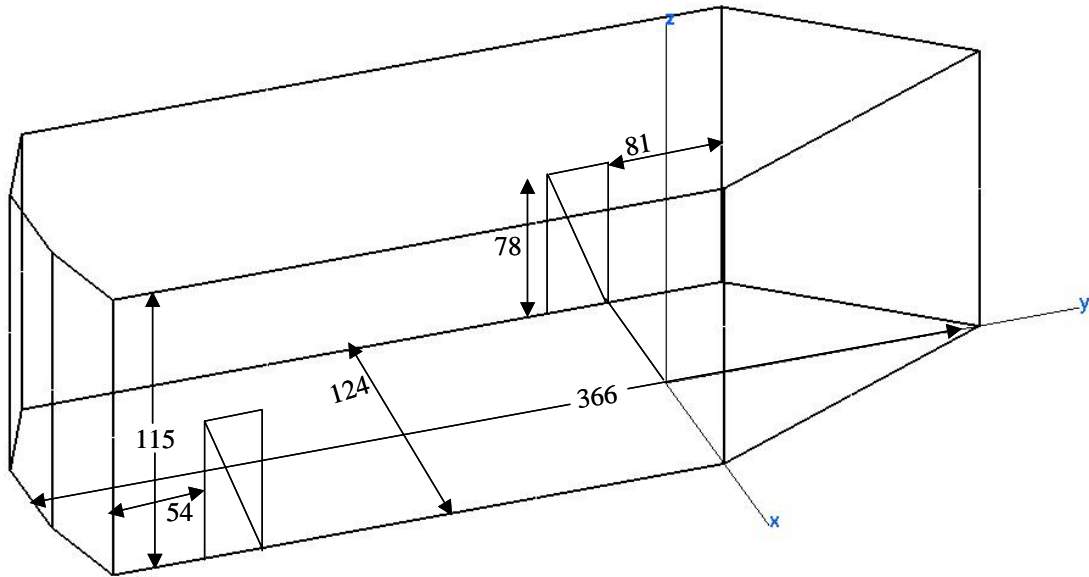


Figure 18. Specification of the anechoic chamber at the Naval Postgraduate School, Monterey, CA (Spanagel Hall Room 604)

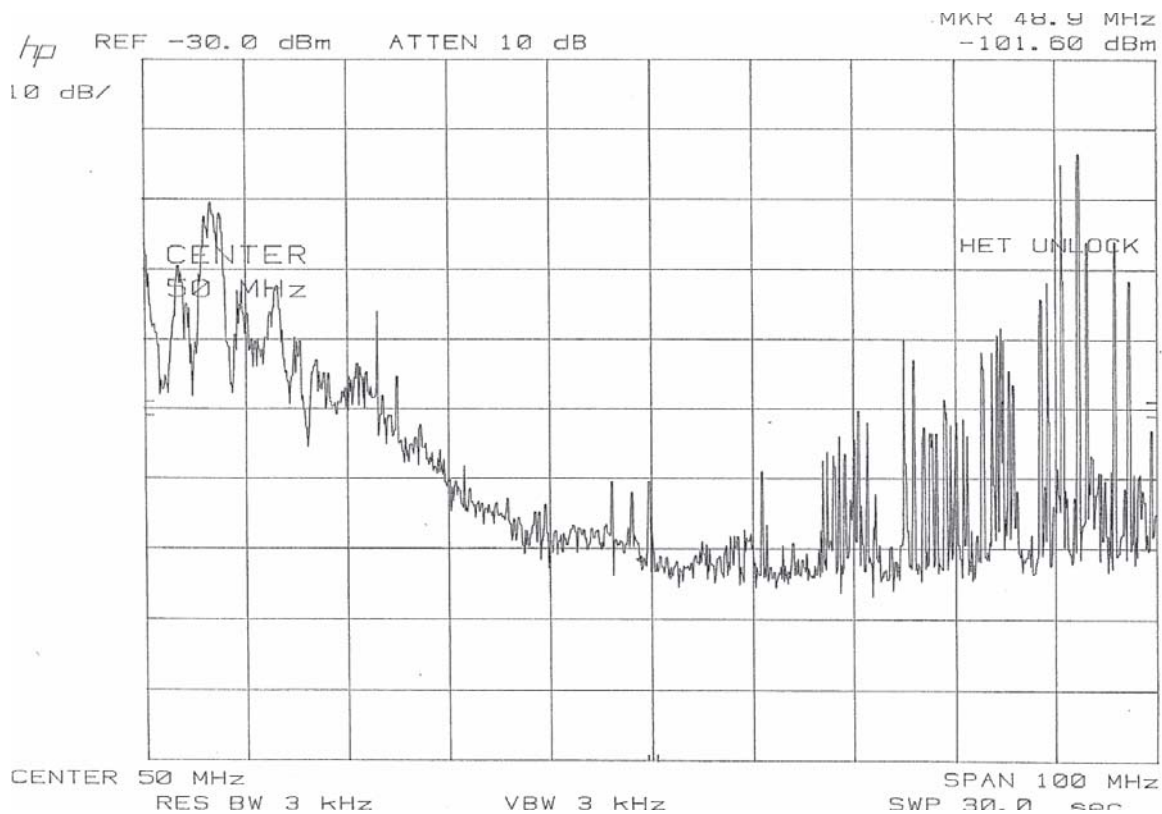


Figure 19. The noise measurement in 0-100 MHz frequency range for the Naval Postgraduate School anechoic chamber

G. SUMMARY

This chapter presented basic RAM theory, different types of RAM structures, anechoic chamber absorber types, and some information about the NPS anechoic chamber.

The objective of RAM design is to find the appropriate material that gives the highest attenuation within the RAM thickness limits. It is difficult to satisfy both requirements simultaneously since high loss materials have intrinsic impedances much different from that of free space, and thus suffer high front-face reflections. Tapering the loss from the front to the back of the absorber (i.e. geometric absorbers) can solve some of these problems, but each solution has its own advantages and disadvantages.

Anechoic chambers are vital for testing and measurement of equipment and platforms. In Chapter IV, the simulations and their results will be presented for the NPS

anechoic chamber for a uniformly excited circular aperture antenna, and different types of absorbers by using the Urbana Wireless Toolset.

IV. URBANA SIMULATIONS

In this chapter, the anechoic chamber in the Naval Postgraduate School has been modeled and simulated with different types of absorbers by using a uniform circular aperture antenna. To create the model and generate the field contours, the process in Figure 11 of Chapter II is used. In the following sections the steps for generating the simulations and the simulation results will be illustrated.

A. INPUT DATA FOR THE SIMULATIONS

1. Geometrical Model

The Urbana wireless toolset uses triangular facets for representing geometrical models. The anechoic chamber model has been generated and faceted by using ACAD software. The Length unit has been chosen as inches. The detailed dimensions of the chamber were illustrated in Figure 18 and the faceted model is illustrated in Figure 20.

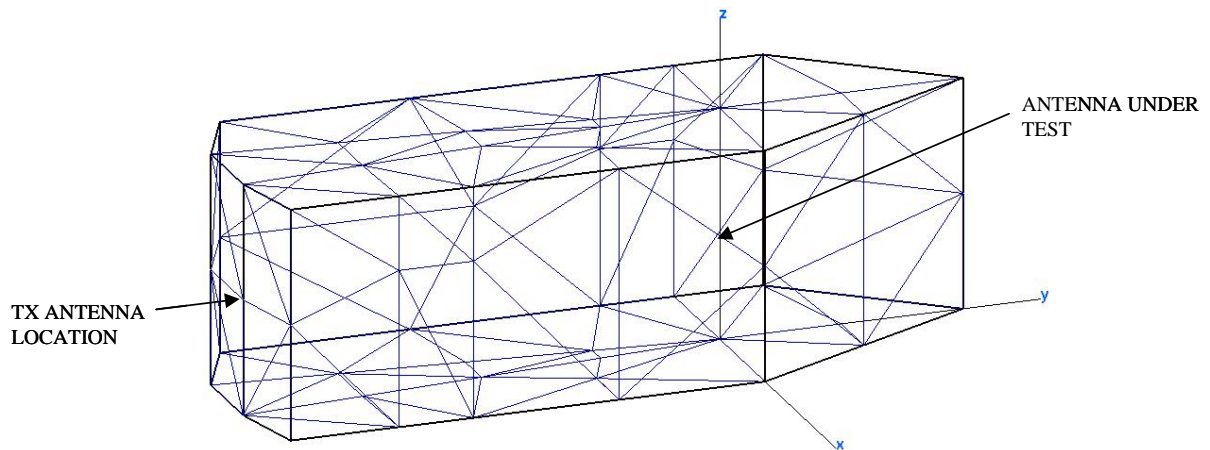


Figure 20. Naval Postgraduate School anechoic chamber facet model

The material specifications for each facet are specified by the ICOAT variable. Different ICOAT values have been used for these simulations depending on the absorber type.

2. Antenna Pattern File

An antenna that has a physical circular shaped aperture is called a circular aperture antenna. It has a simple configuration and structure. One of the most commonly used antenna types is the circular aperture. For anechoic chamber simulations a uniform circular aperture antenna has been used.

The ideal uniform circular aperture has constant amplitude distribution. The antenna aperture radius (a) defines the half power beamwidth of the antenna. The half power beamwidth is given as $\text{HPBW} = 58.4(\lambda / 2a)$ degrees and the directivity is given as $D = 4\pi^2 a^2 / \lambda^2$ where λ is the wavelength. The sidelobe level of any uniform circular aperture pattern is -17.6 dB. The normalized pattern of a uniform circular aperture is [13]

$$f(\theta) = \frac{2J_1(\beta a \sin \theta)}{\beta a \sin \theta} \quad (4.1)$$

where J_1 is the first order Bessel function. The antenna pattern is shown in Figure 21 for a 15 degree HPBW.

The antenna pattern file is created by using MATLAB and then translated into the Urbana antenna file format. The antenna is located at (0,242,58). The location of the antenna is shown in Figure 20. The MATLAB code is shown in Appendix C. The simulations are performed for 15 and 20 degrees half power beamwidths at 2.0 GHz. Two different kinds of absorbers are used.

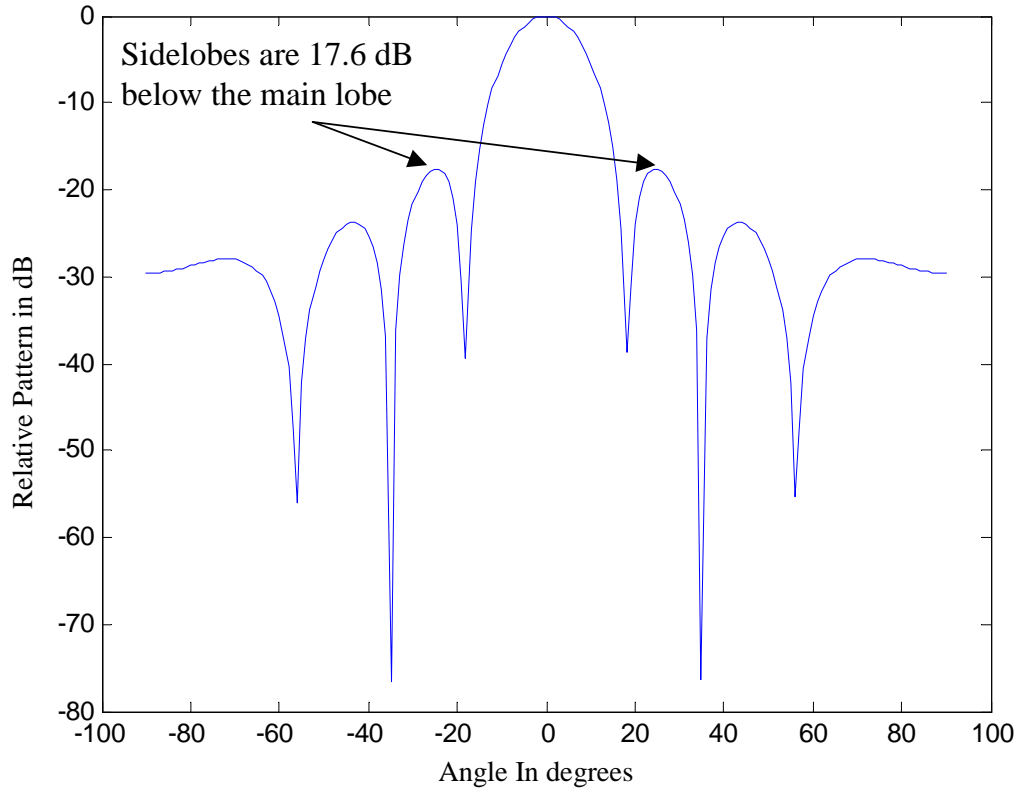


Figure 21. Uniform circular aperture antenna pattern for 15 degree HPBW, normalized by directivity ($a = 0.243\text{m}$ / $D = 21.75\text{ dB}$)

3. Absorber Selection

For simulating the anechoic chamber absorber, two kinds of Dallenbach layers have been designed. These designs do not necessarily represent real materials, but their reflection coefficient values are in the range of actual absorbing materials described in Table 2 in Chapter III.

The backing material for the absorbers is assumed as PEC, so the Z_{LOAD} value in Equation (3.10) is taken as zero. The reflection coefficients are calculated by using Equations (3.9) and (3.10). The permittivity is assumed as $\mu_r = 1 + j0$ and the real part of permittivity is assumed as $\epsilon'_r = 4$. The imaginary part of permittivity (ϵ''_r) has been changed to achieve reflection coefficients of -8.3 dB and -27 dB . The thickness is assumed as 2.24 inches. The absorber reflectivity values are shown in Figure 22. For the

−8.3 dB absorber $\epsilon_r'' = 3$, and for −27 dB absorber $\epsilon_r'' = 1$ is used. In the latter case the material is acting like a quarter-wave matching plate.

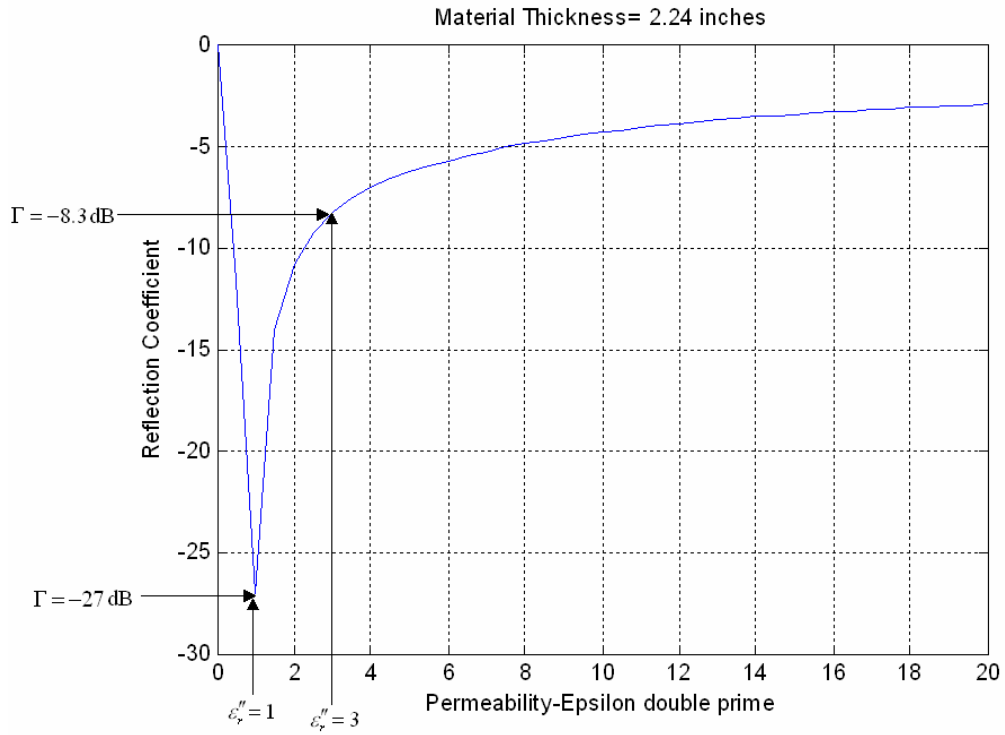


Figure 22. Reflectivity curve of the designed absorbers

A MATLAB code was created for calculating the reflectivity values and it is shown in the Appendix C.

B. INPUT FILE GENERATION AND DISPLAYING THE RESULTS

Using the parameters provided in the input file, Urbana calculates the electric fields for observation points and creates a field file. Table 4 shows some of the simulation parameters in the Urbana input file.

Input Parameters	VALUES
Facet Model	chamberconv.facet
Unit Length	inches
Frequency	2.0 GHz
Antenna Description	from file:antenna.txt
Antenna Type	Circular Aperture
Antenna Polarization	Vertical X(0, 0, 1) and Z(0, 1, 0)
Observation Points	from file:observe.txt
Computation Method	Geometrical Optics
Edge Diffraction	GTD
Edge File	chamberconv.edge
Angular Interval	1.0 Degrees
Max Ray Bouncing	5
Coating Material	Absorbing Material
Advanced features	OFF

Table 4. Sample Urbana Input Parameters

For displaying the results, the f2f.x (field to facet) program is used. The field file created by Urbana is converted to a facet file which can be displayed by Xcell. Table 5 shows the input parameters for running f2f.x.

Input Parameters	VALUES
Type of E-Field	Magnitude of E-Total
Number of Field Files	1
Name of Field File	chamber6.field
Antenna Power Level	1
Histogram Interval	10 dB
Max. and Min. Clip Values	-40 to 60 dBm'
Max. and Min. Range Value	-10 to 60 dBm'
Number of Levels	25
Lowest Coating Code	1
Name of Output Facet File	chamber6.facet
Side of Footprint Square	2
Shift According to Z-data	N
Enter z-offset footprint	0

Table 5. Sample f2f.x input parameters

The displayed data from f2f.x consists of color-coded power contours. These contours represent the signal strength in dBm values. All contours for the chamber simulations are at a height of 58 inches.

C. SIMULATIONS OF THE EMPTY CHAMBER

1. Initial Urbana Simulations

After designing the geometrical model of the NPS anechoic chamber and creating the input file, a test case was run in order to see the antenna pattern and validate the input file data. The inside walls of the chamber are covered with a perfect absorber which is ICOAT=1. This material is defined internally in Urbana. A perfect absorbing surface has no reflected rays leaving the surface. Urbana guarantees this by terminating rays that hit an absorbing surface. A uniform circular aperture with a 15 degree HPBW is used for this case at a frequency of 2.0 GHz.

Two different simulations were run, one for a vertically polarized antenna and one for horizontally polarized antenna. The first case is for vertical polarization, shown in Figure 23. The main beam and the side lobes are clearly seen. The second case, shown in Figure 24 is for horizontal polarization and antenna pattern features (main beam and sidelobes) are clearly visible.

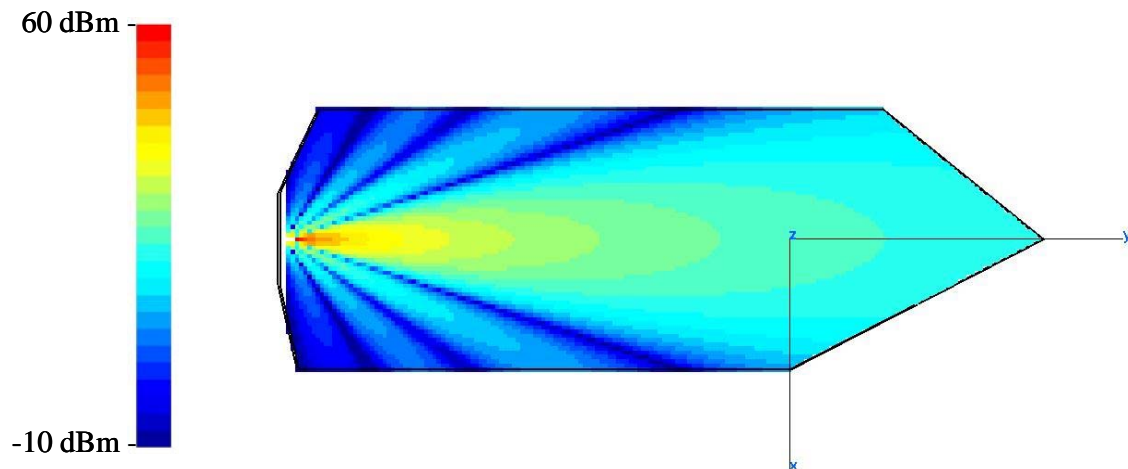


Figure 23. Vertically polarized 15 degree HPBW circular aperture with perfect absorber wall coating ($z=58$ inches).

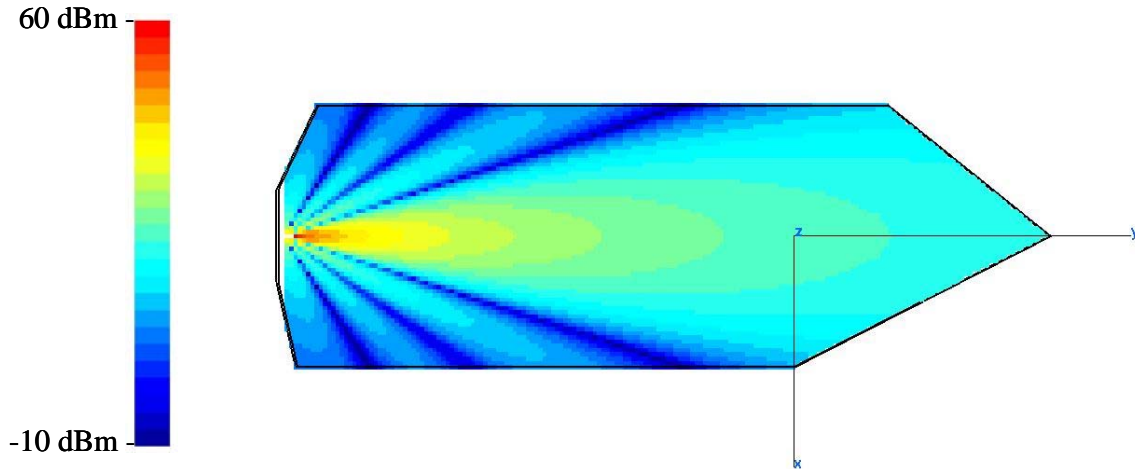


Figure 24. Horizontally polarized 15 degree HPBW circular aperture with perfect absorber wall coating ($z = 58$ inches)

These two simulations validated the antenna pattern file and geometrical model. Next, this antenna pattern and geometrical model will be used for the absorber reflection values of -8.3 dB and -27 dB.

2. Absorber Coated Walls

This section examines the performance of the NPS anechoic chamber with two antenna beamwidths (15 and 20 degrees), and two different absorbers at 2.0 GHz.

The simulation shown in Figure 25 was performed with a vertically polarized circular aperture antenna having a 15 degree HPBW and -8.3 dB absorber coated walls. Since the absorber is not a perfect absorber, the antenna pattern is not as clearly visible as in Figure 23. The absorber effects can especially be seen in the nulls of the antenna pattern. The reflections from the absorbing walls are creating constructive and destructive effects and interference in the nulls. These effects can also be seen clearly in the front part of the anechoic chamber, and for the perfect absorber walls these effects were not present.

The horizontally polarized antenna for the same case is shown in Figure 26 and the destructive and constructive effects can be compared with Figure 24.

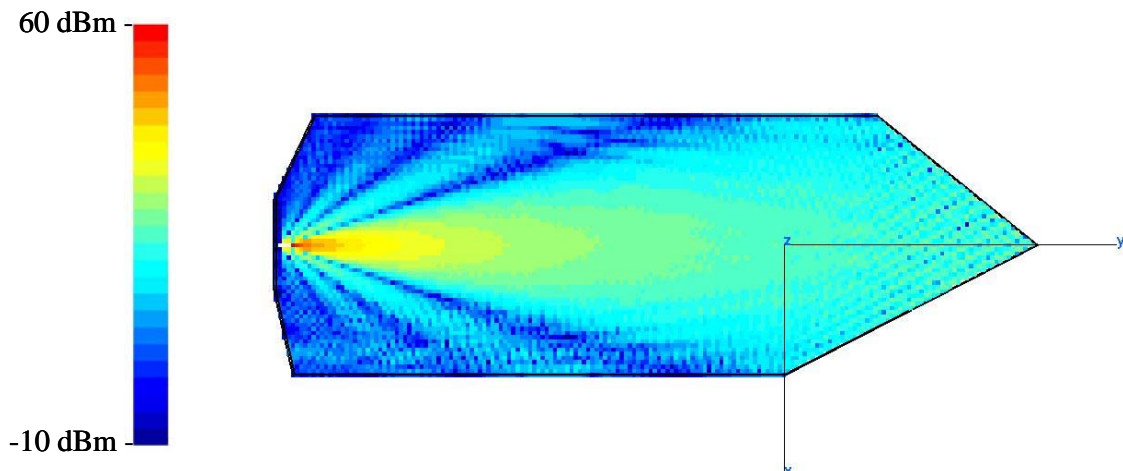


Figure 25. Vertically polarized 15 degree HPBW antenna with -8.3 dB absorber wall coating, total field.

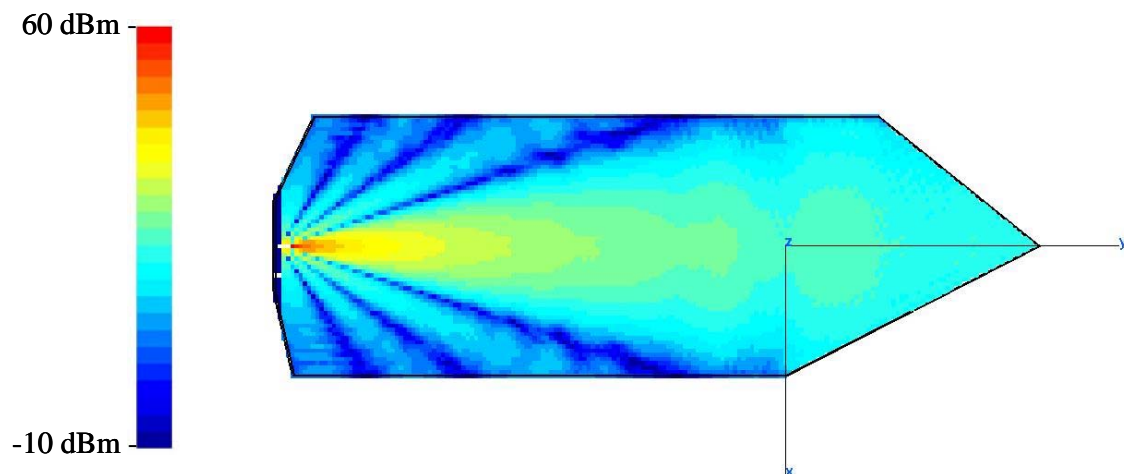


Figure 26. Horizontally polarized 15 degree HPBW antenna with -8.3 dB absorber wall coating, total field.

In order to see the behavior of the reflected energy, these two cases are also simulated without the direct contribution. These two cases are shown in Figure 27 and Figure 28. The signal level went down to the 30 dBm level and the reflected energy can be seen, especially in the right side triangular part of the chamber. This part behaves like a corner reflector and the reflected energy is focused in that region.

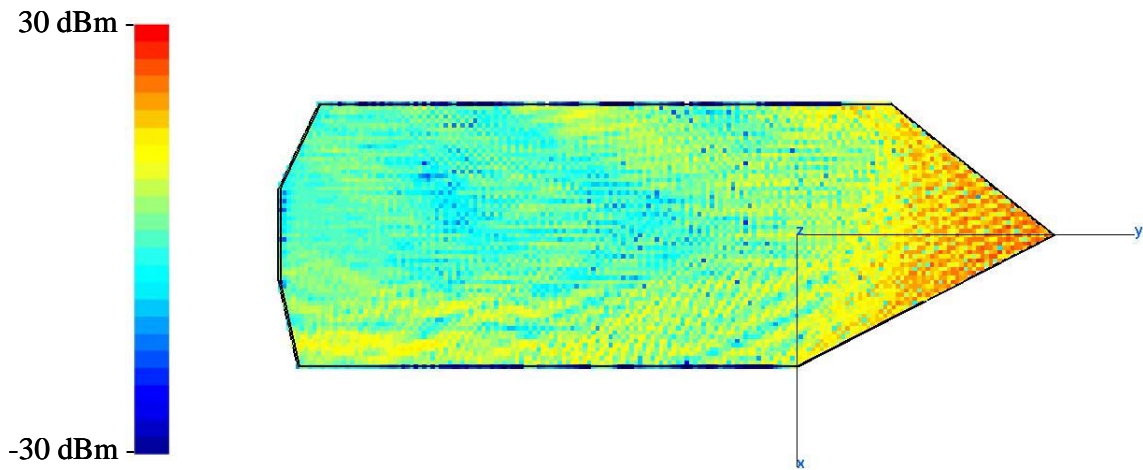


Figure 27. Vertically polarized 15 degree HPBW antenna with -8.3 dB absorber wall coating, reflections only.

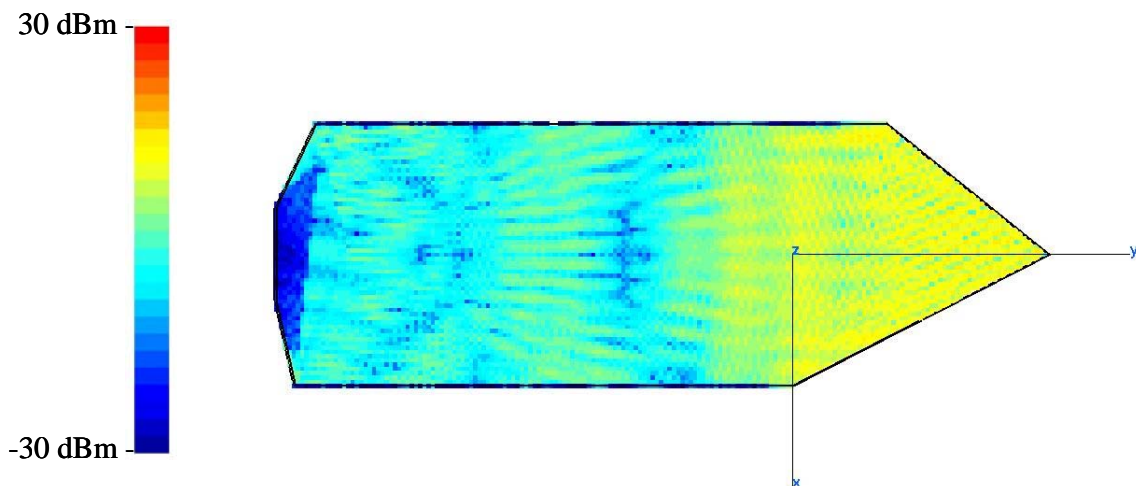


Figure 28. Horizontally polarized 15 degree HPBW antenna with -8.3 dB absorber wall coating, reflections only

For the next simulations, the antenna HPBW is changed to 20 degrees and the same -8.3 dBm absorber coating is used. The same cases as for the previous simulations have been repeated. The results are shown in Figures 29 to 32. The HPBW difference can be seen clearly from the width of the main lobe and side lobes. The reflection effects on the pattern can also be seen in the figures.

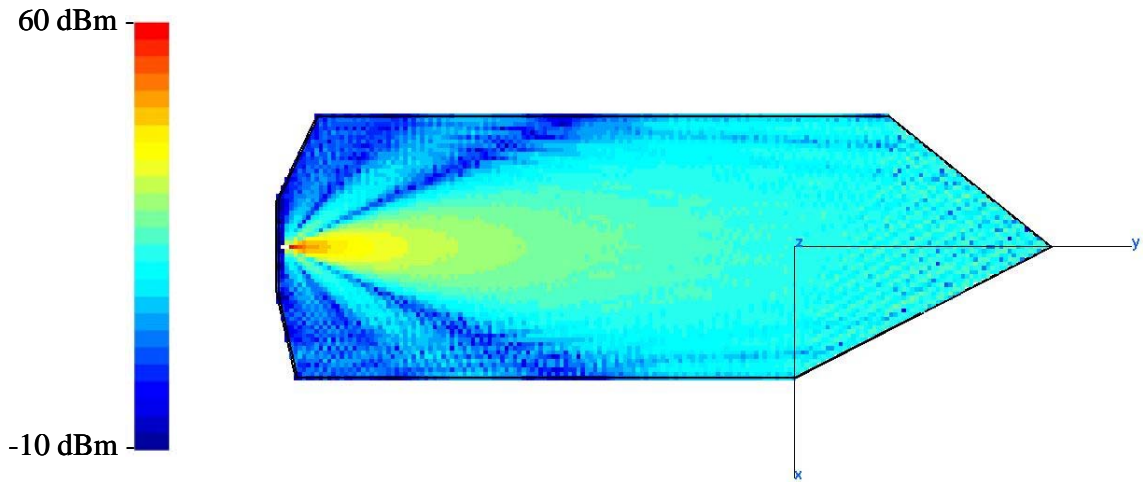


Figure 29. Vertically polarized 20 degree HPBW antenna with -8.3 dB absorber wall coating, total field.

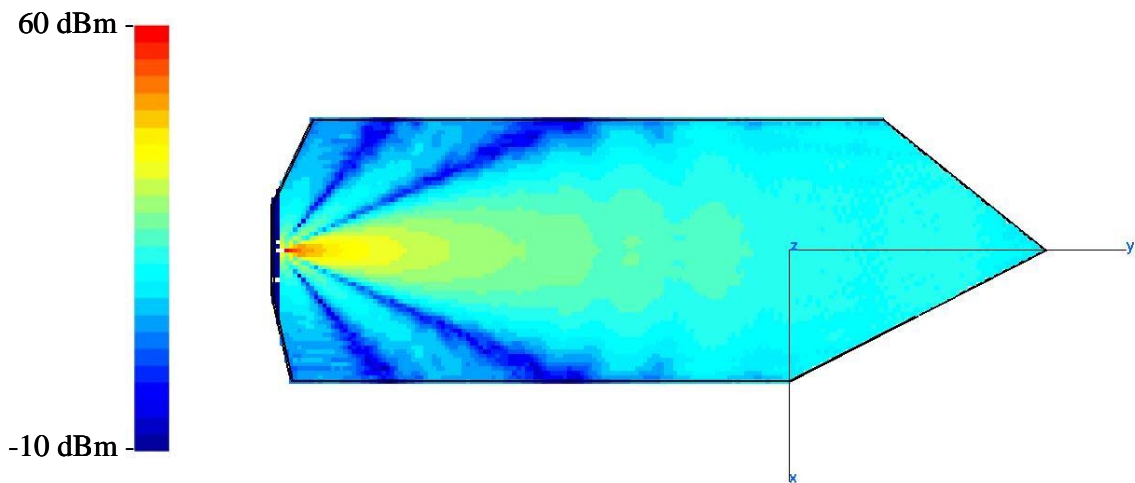


Figure 30. Horizontally polarized 20 degree HPBW antenna with -8.3 dB absorber wall coating, total field.

Figures 31 and 32 show the reflected waves for the 20 degree HPBW case, and appear very similar to the reflection effects for the 15 degree HPBW case.

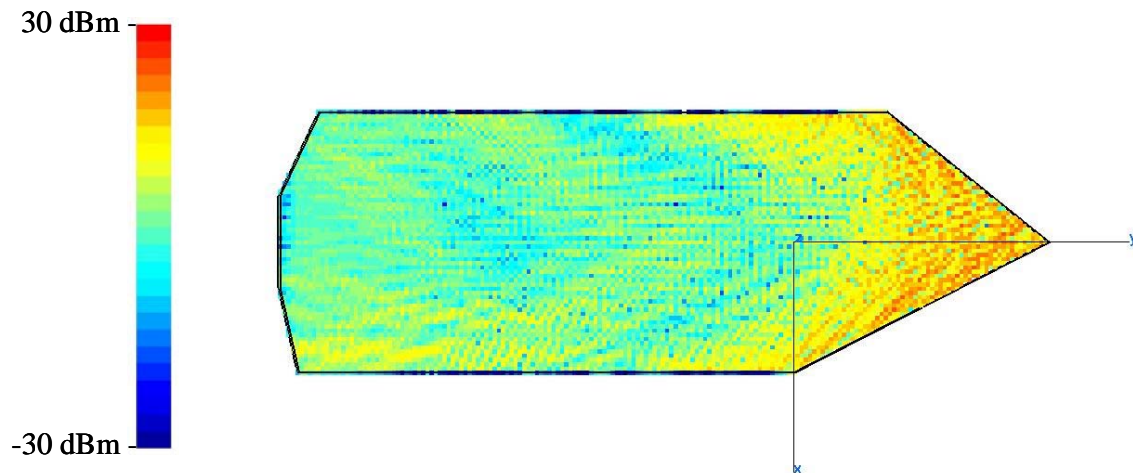


Figure 31. Vertically polarized 20 degree HPBW antenna with -8.3 dB absorber wall coating, reflections only.

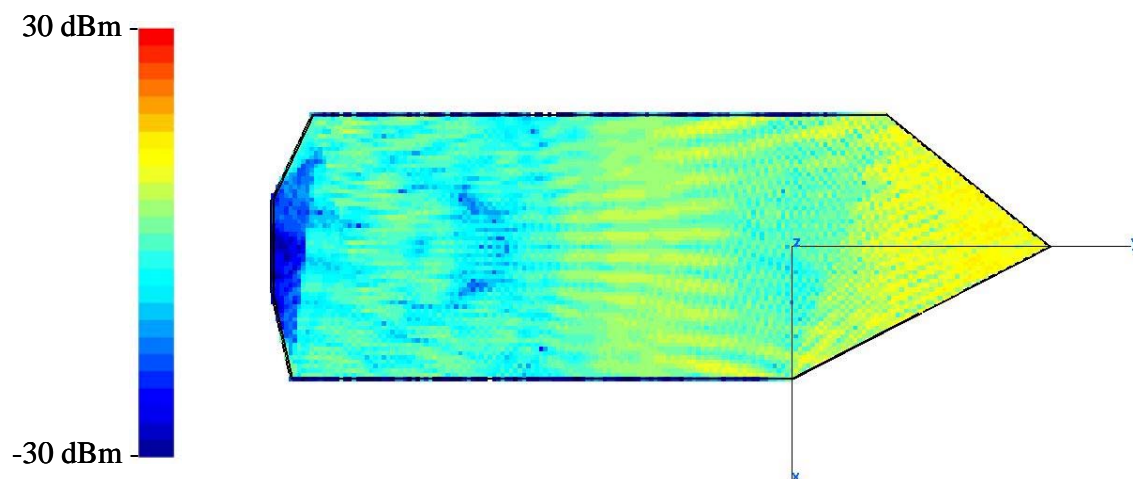


Figure 32. Horizontally polarized 20 degree HPBW antenna with -8.3 dB absorber wall coating, reflections only.

Thus, the -8.3 dB absorber effects for 15 and 20 degree HPBW's have been examined for vertical and horizontal polarization. Next, the -27 dB absorber will be used for these cases, and the results will be examined. Figures 33 and 34 show the 15 degree HPBW antenna pattern for the -27 dB absorber.

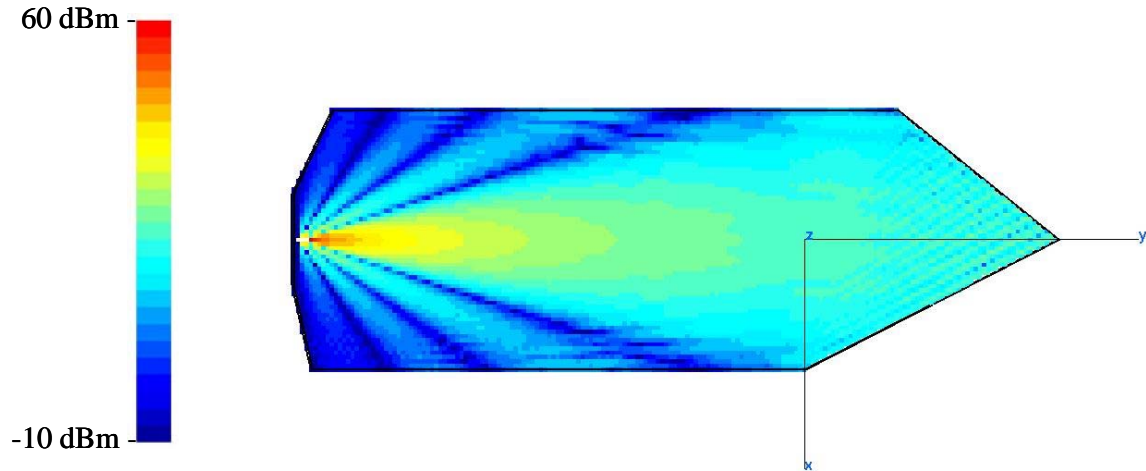


Figure 33. Vertically polarized 15 degree HPBW antenna with -27 dB absorber wall coating, total field.

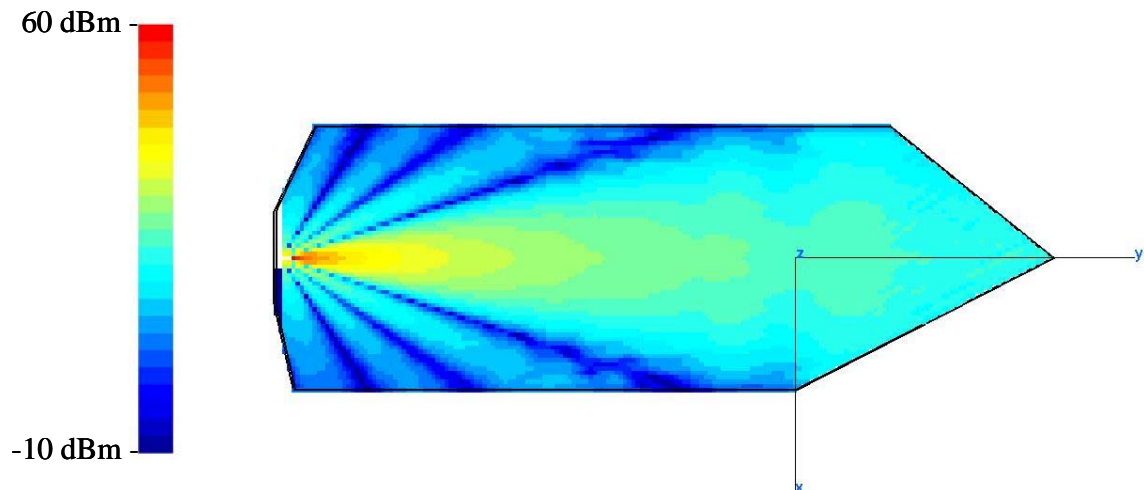


Figure 34. Horizontally polarized 15 degree HPBW antenna with -27 dB absorber wall coating, total field.

Since the -27 dB absorber has a lower reflection coefficient and less of the incident energy is reflected, there is less interference than the -8.3 dB absorber case. This can be seen in the antenna pattern and the front part of the room for both polarizations (more uniform colors). Figures 35 and 36 show the reflections only for the -27 dB absorber. The reflected field power level is lower than -8.3 dB case, as expected, and it can be seen from the color-coded power contours.

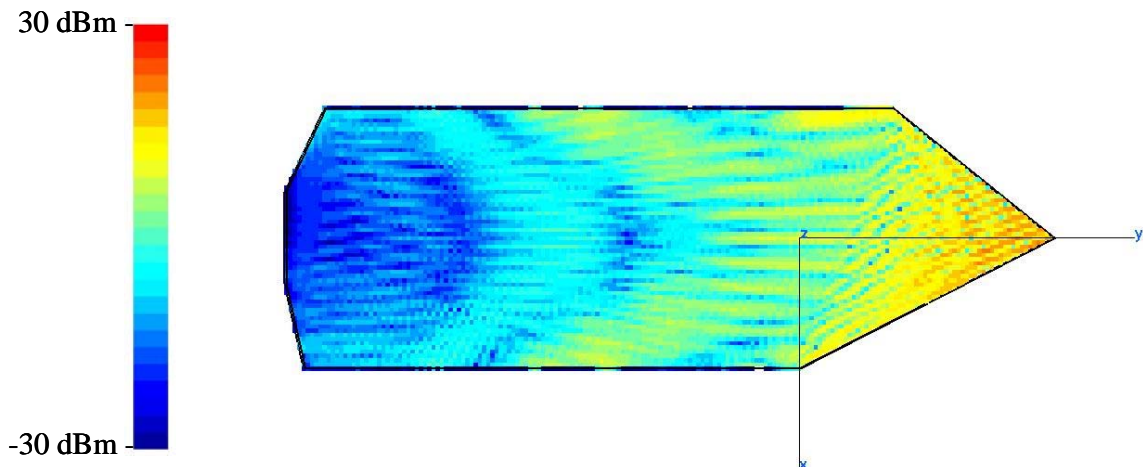


Figure 35. Vertically polarized 15 degree HPBW antenna with -27 dB absorber wall coating, reflections only.

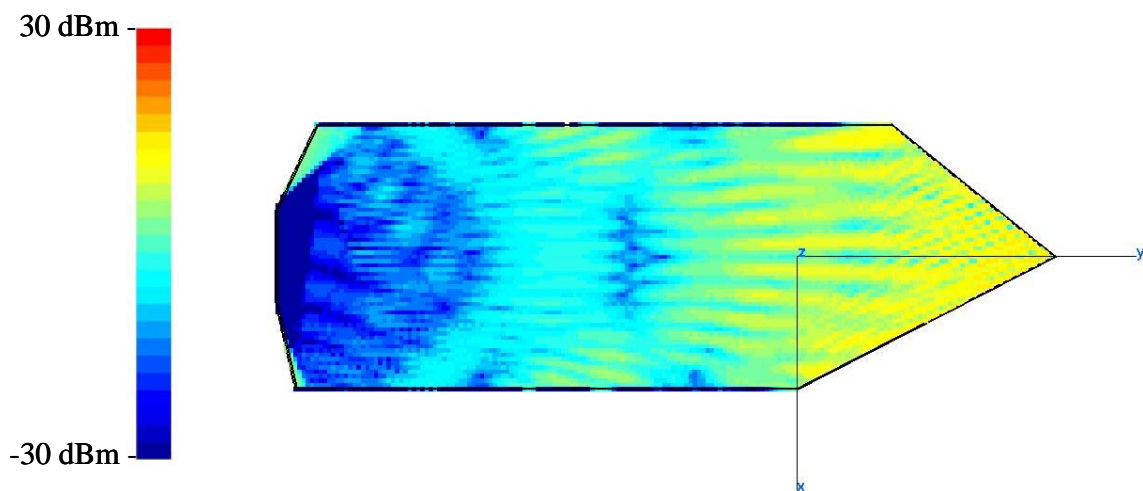


Figure 36. Horizontally polarized 15 degree HPBW antenna with -27 dB absorber wall coating, reflections only.

The 20 degree HPBW antenna case is also simulated for the -27 dB absorber. Figures 37 and 38 show the antenna pattern for the 20 degree HPBW case. The main beam, sidelobe and the interference effects can be seen clearly in the figures.

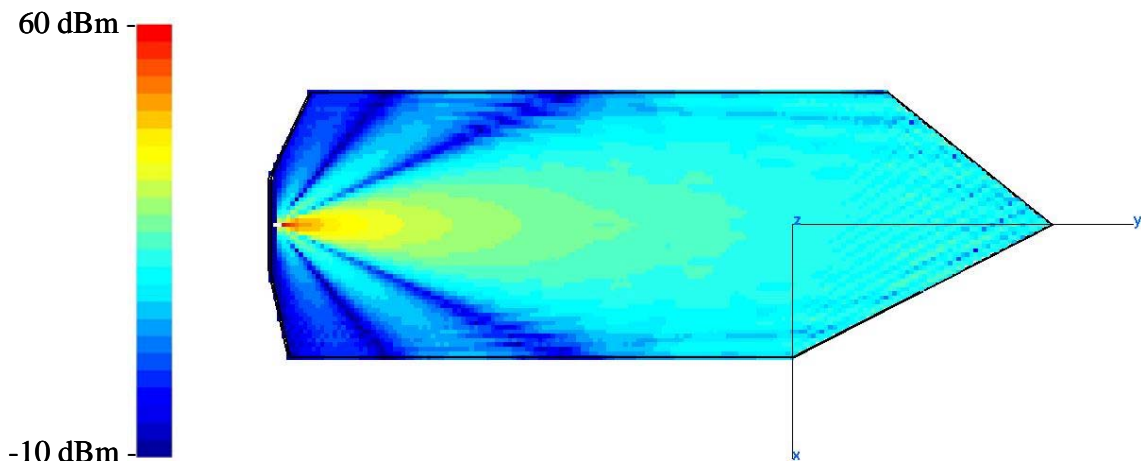


Figure 37. Vertically polarized 20 degree HPBW antenna with -27 dB absorber wall coating, total field.

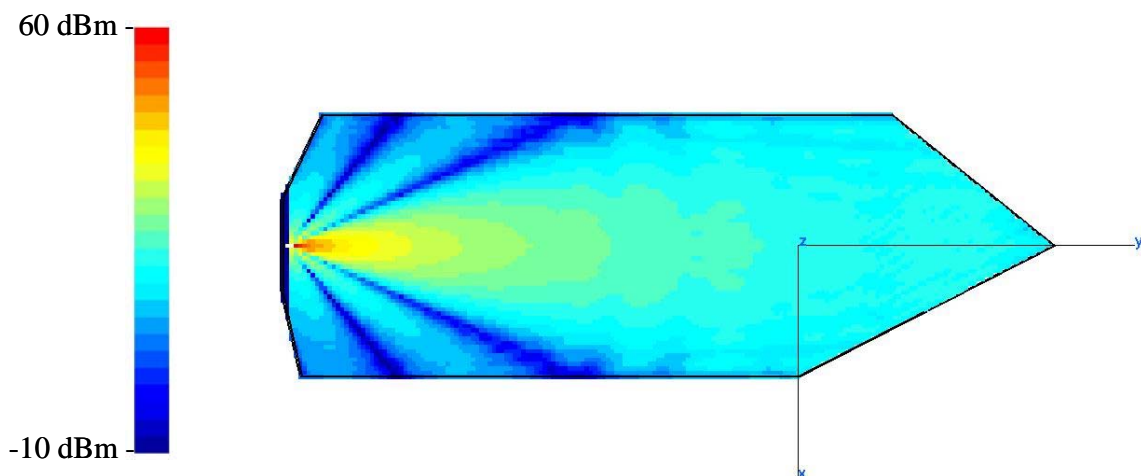


Figure 38. Horizontally polarized 20 degree HPBW antenna with -27 dB absorber wall coating, total field.

The reflection only case for a 20 degree HPBW is shown in Figures 37 and 38. The reflections from the main beam can be seen better than for the 15 degree HPBW. The wider beam allows more illumination of the side walls.

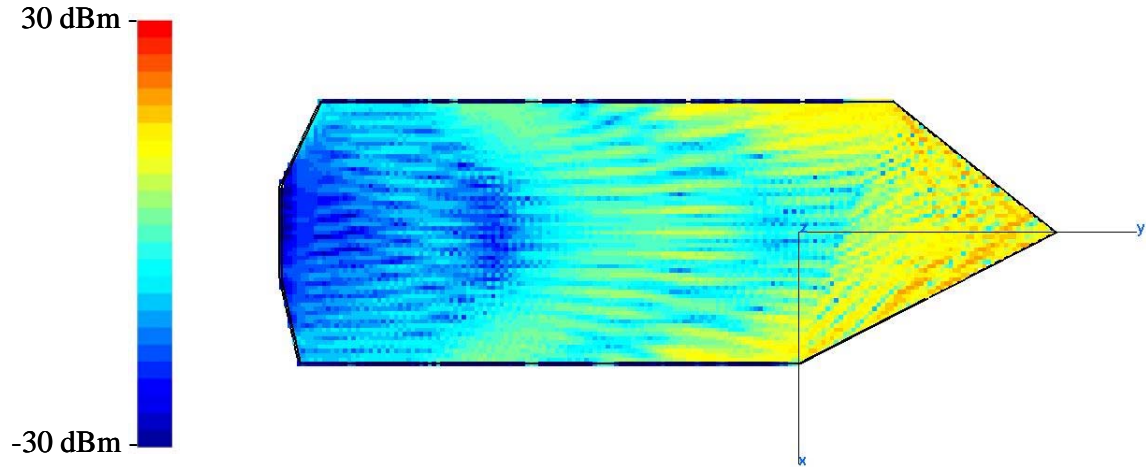


Figure 39. Vertically polarized 20 degree HPBW antenna with -27 dB absorber wall coating, reflections only.

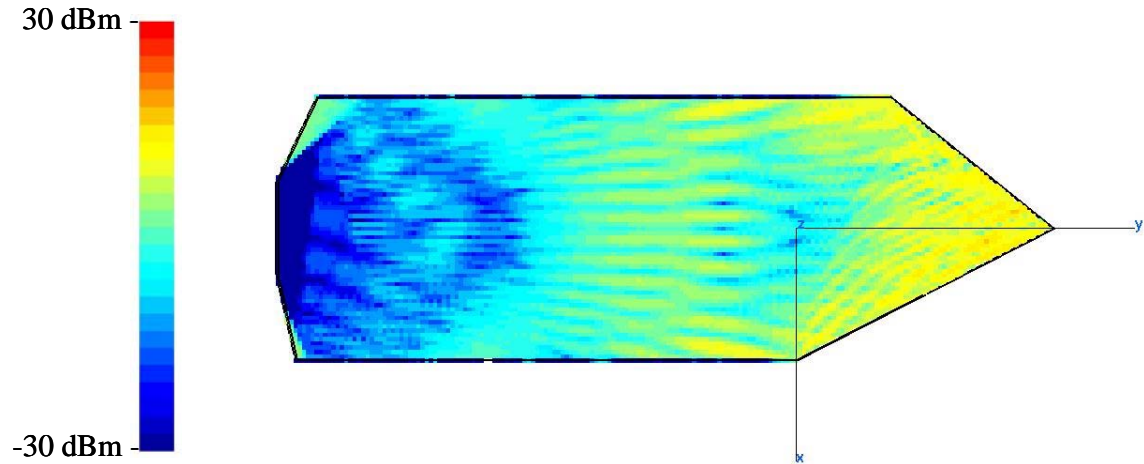


Figure 40. Horizontally polarized 20 degree HPBW antenna with -27 dB absorber wall coating, reflections only.

D. ESTIMATION OF THE QUIET ZONE

The transmitted wave from the antenna is a spherical wave in the antenna far field. For measurement of antenna gain, a plane wave should be incident on the antenna. Similarly, for the measurement of radar cross section (RCS) a plane wave is desired at the target. Therefore separation between the antenna and target should be large enough to ignore the difference between an ideal plane wave and the actual spherical wave. The area of the chamber over which the plane wave approximation is valid, is called its quiet zone. It is a function of the transmit antenna beamwidth and test range, R . For the current

chamber configuration, $R = 242$ inches. If the test object length is L , as illustrated in Figure 41, the phase error at the edge of the target relative to the center is

$$k\Delta_{\max} = k[\sqrt{R^2 + (L/2)^2} - R] \approx \frac{\pi L^2}{4R\lambda} \quad (4.1)$$

The approximation assumes that $L \ll R$.

In addition to a plane phase front at the target, the amplitude of the incident wave across the target must be constant. The amplitude distribution is controlled by the antenna beamwidth and the ratio L/R [2]. The amplitude error is calculated by using a gaussian beam approximation and it is expressed as

$$G(\theta) = Ge^{-2.776(\theta/\theta_{HPBW})^2} \quad (4.2)$$

where G is the antenna gain, θ is the half angle subtended by the test object and θ_{HPBW} is the half power beamwidth (HPBW).

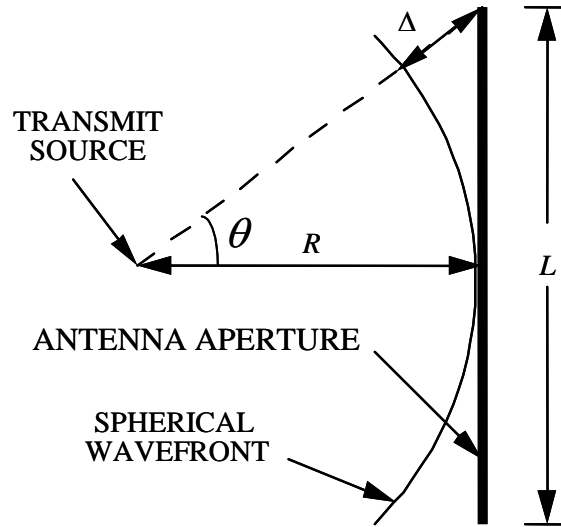


Figure 41. Phase error limitation for a far-field measurement (After Ref. [2]).

In order to avoid the phase and amplitude errors, a MATLAB code is written to check the phase and amplitude error for different beamwidths and aperture sizes. Figure 42 shows the phase error for different aperture sizes and Figure 43 shows the amplitude error for

different aperture sizes and HPBW. The MATLAB code is given in the Appendix C.

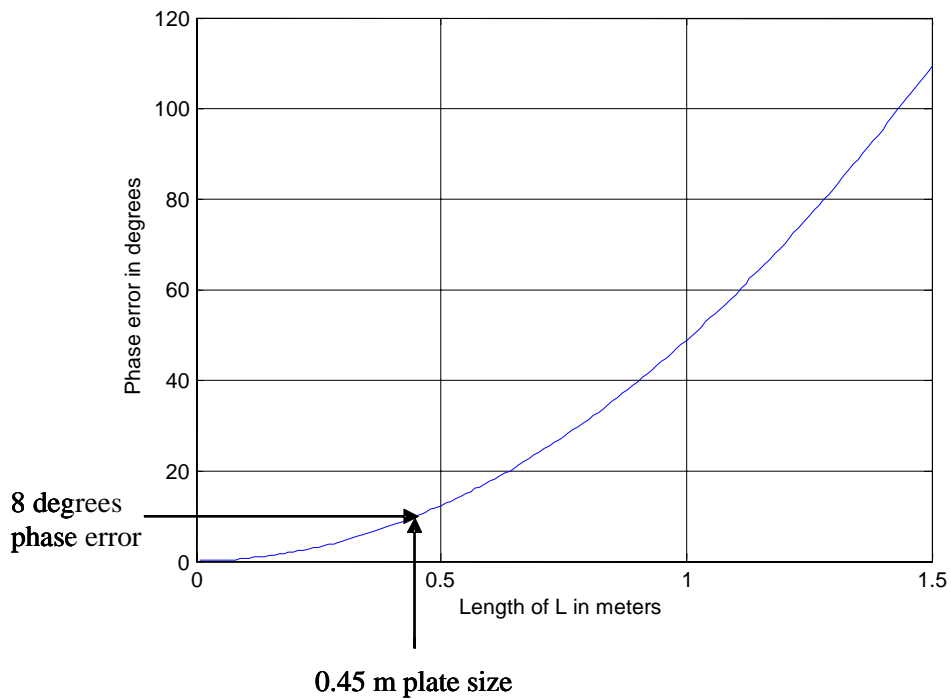


Figure 42. Phase error in degrees

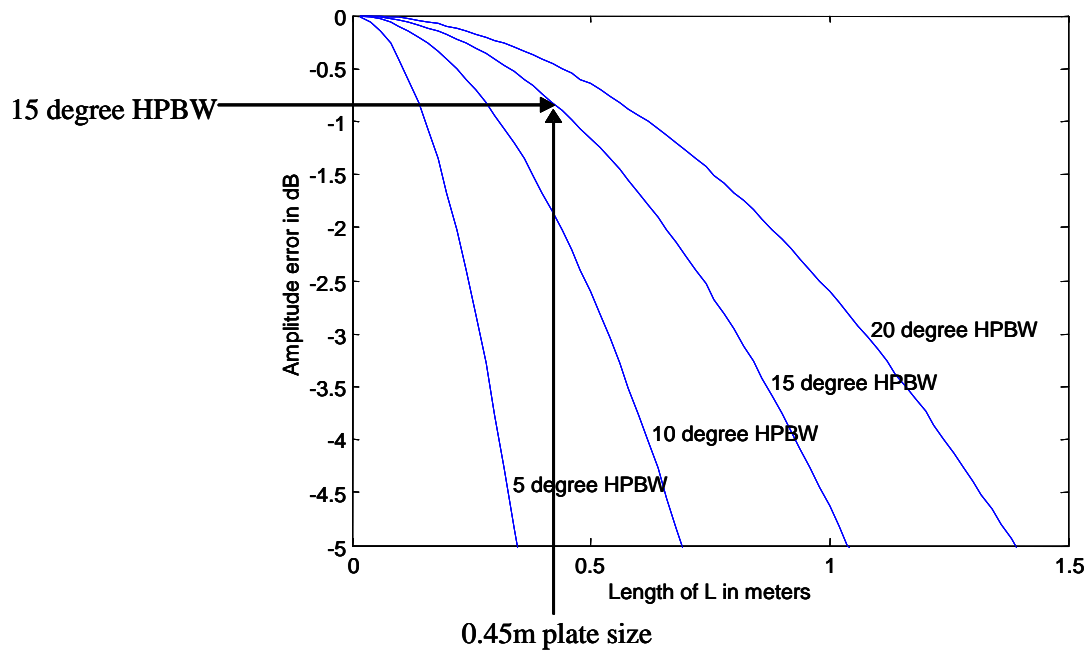


Figure 43. Amplitude error in dB

E. SIMULATIONS WITH OBJECTS IN THE CHAMBER

1. Perfect Electric Conductor (PEC) Plate in the Chamber

In order to see the strength of the propagation mechanisms in the NPS anechoic chamber, a PEC square plate is placed inside of the chamber at $(0,0,0)$. The plate length is chosen as $L = 0.45$ m to keep the phase error less than 8 degrees and the amplitude error less than 1 dB.

The first simulations were performed for the -8.3 dB absorber and a 15 degree HPBW. Figure 44 illustrates the plate in the chamber for the -8.3 dB absorber and vertical polarization. The reflections from the plate can be seen clearly and there is also a low signal strength region (shadow) behind the plate. The same simulation was performed with edge diffraction included, and the result is shown in Figure 45. The edge diffraction effects from the plate can be seen in the figure as an increase in the angular spread of energy reflected from the plate.

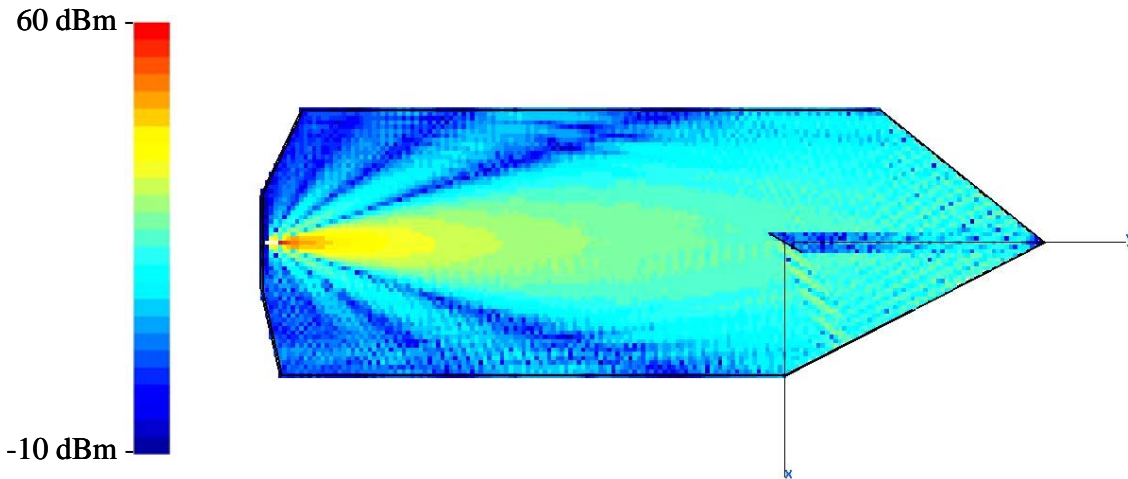


Figure 44. Vertically polarized 15 degree HPBW antenna with -8.3 dB absorber with a PEC plate, total field.

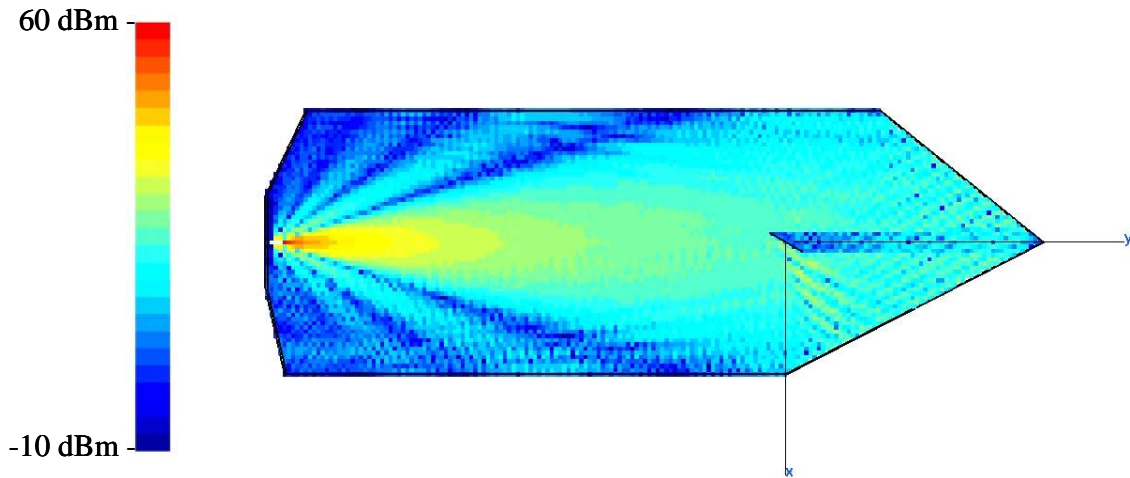


Figure 45. Vertically polarized 15 degree HPBW antenna with -8.3 dB absorber with a PEC plate and edge diffraction included, total field.

To examine the reflection and diffraction in more detail, the direct contribution is suppressed. Figures 46 and 47 show the same case for no direct contribution, with and without edge diffraction effects. The reflection from the plate, the walls and edge diffraction effects can be seen clearly. After a few reflections from the plate and walls the reflected wave energy fades away.

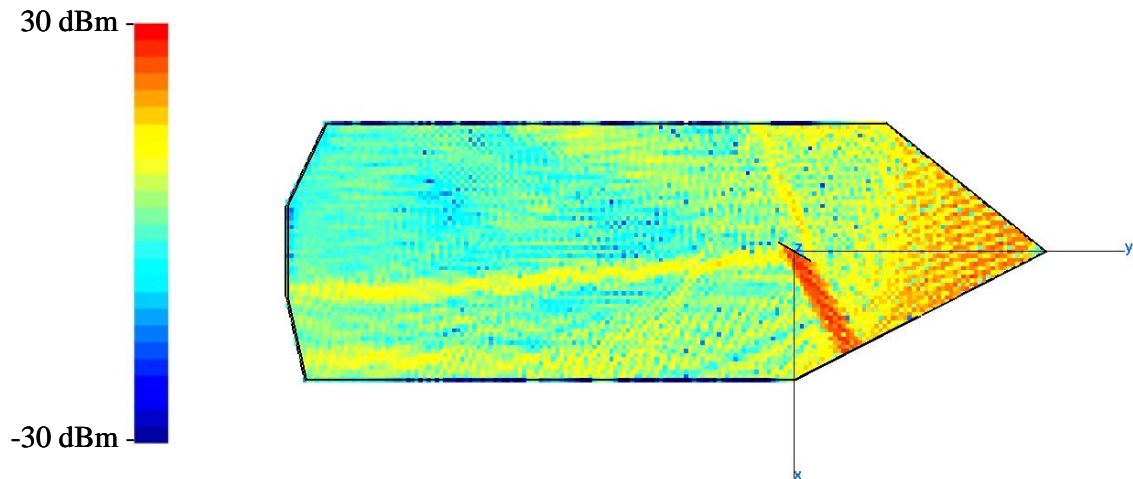


Figure 46. Vertically polarized 15 degree HPBW antenna with -8.3 dB absorber, no direct contribution with a PEC plate.

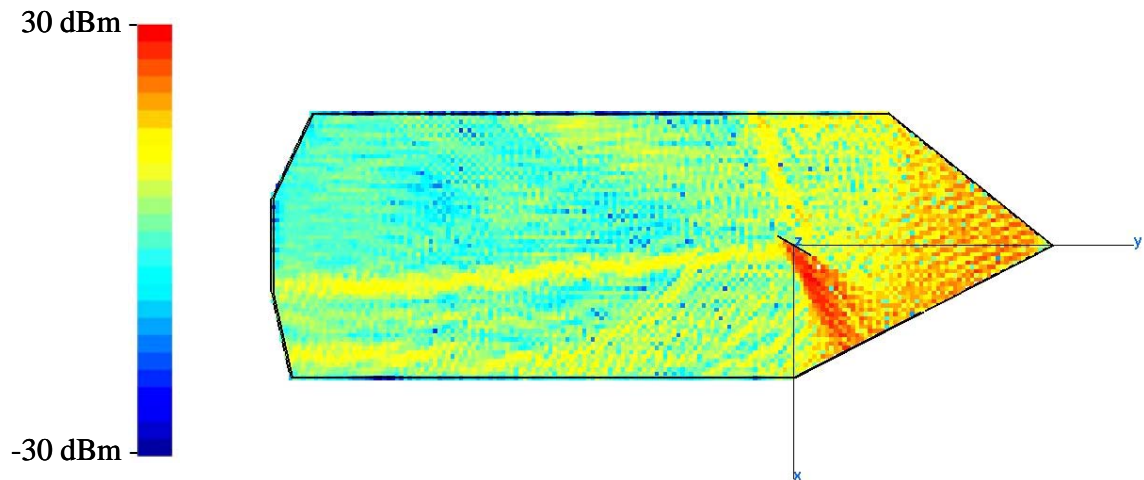


Figure 47. Vertically polarized 15 degree HPBW antenna with -8.3 dB absorber, no direct contribution with a PEC plate and edge diffraction included.

The same simulations are performed for a horizontally polarized antenna and the simulation results are shown in Figures 48 through 51. In general, reflections for the horizontally polarized case are lower than for vertical polarization case.

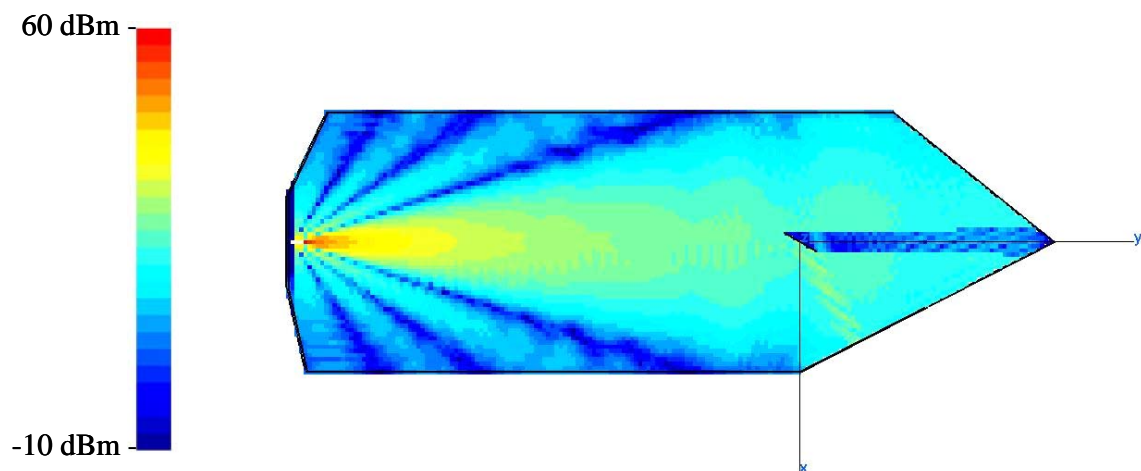


Figure 48. Horizontally polarized 15 degree HPBW antenna with -8.3 dB absorber with PEC plate, total field.

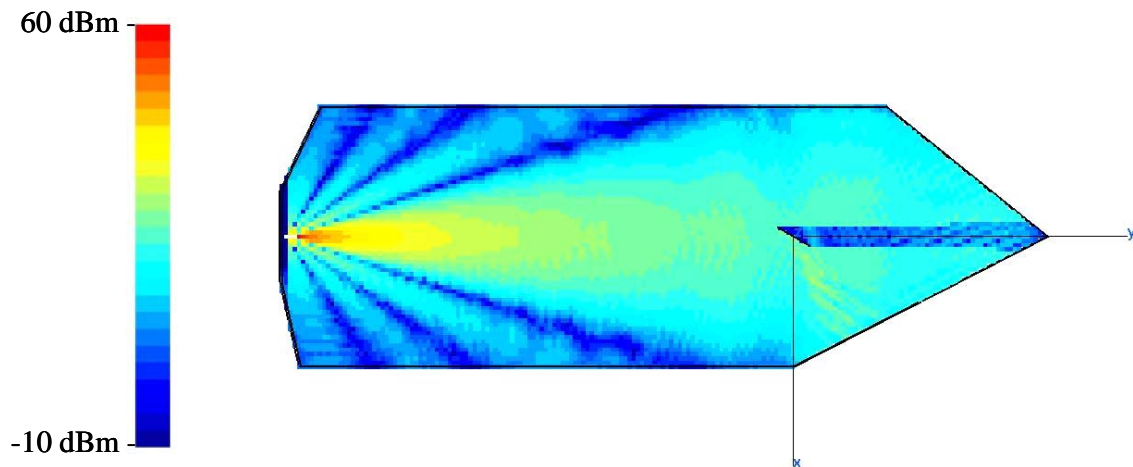


Figure 49. Horizontally polarized 15 degree HPBW antenna with -8.3 dB absorber with a PEC plate and edge diffraction included, total field.

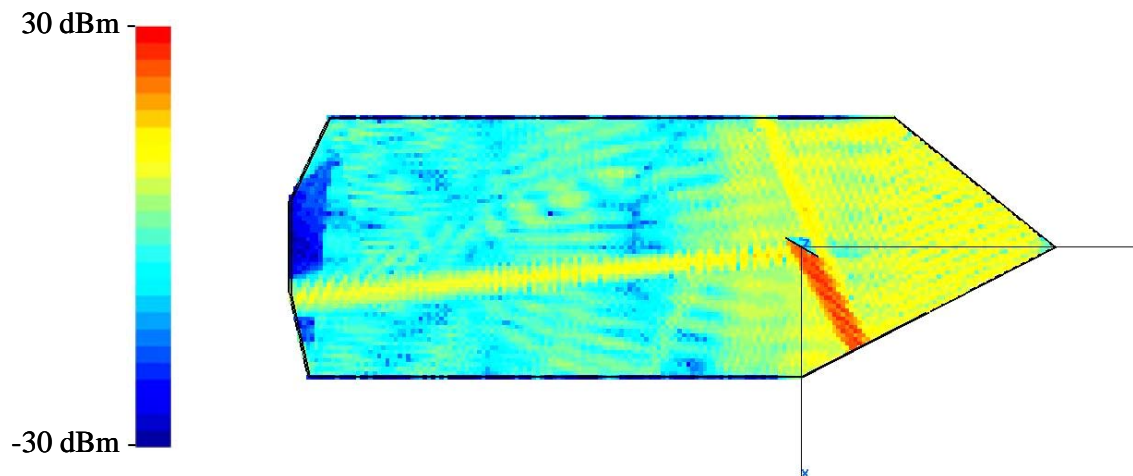


Figure 50. Horizontally polarized 15 degree HPBW antenna with -8.3 dB absorber, no direct contribution with a PEC plate.

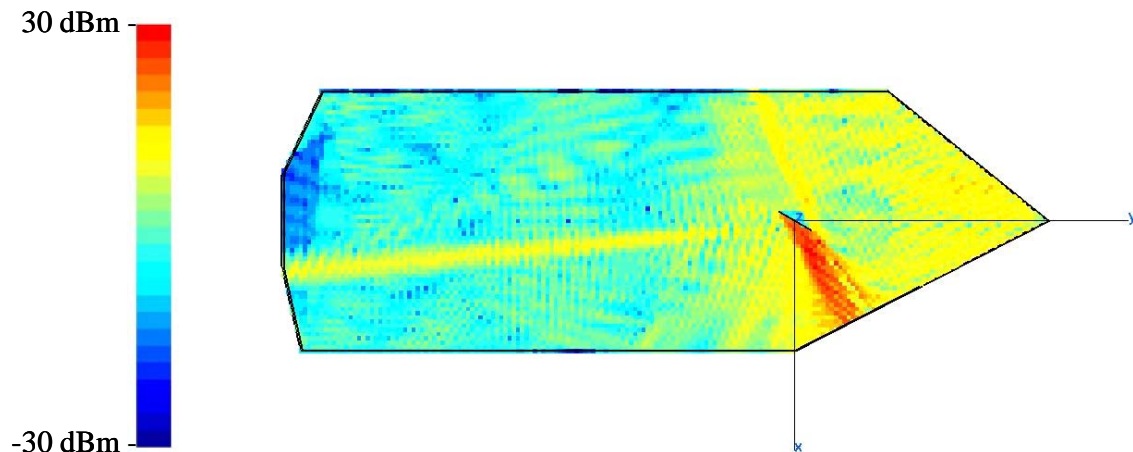


Figure 51. Horizontally polarized 15 degree HPBW antenna with -8.3 dB absorber, no direct contribution with a PEC plate and edge diffraction included.

Next, the absorber type is changed to the -27 dB absorber. Figures 52 and 53 illustrate the vertically polarized antenna with the plate. The difference from the -8.3 dB absorber case cannot be seen clearly because the direct contribution is much larger than the reflections from the walls.

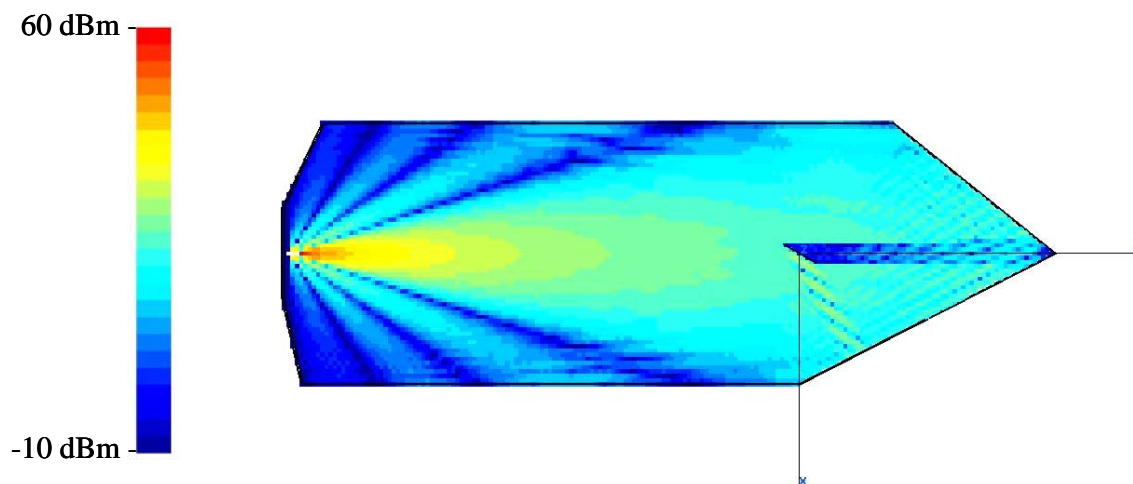


Figure 52. Vertically polarized 15 degree HPBW antenna with -27 dB absorber with a PEC plate, total field.

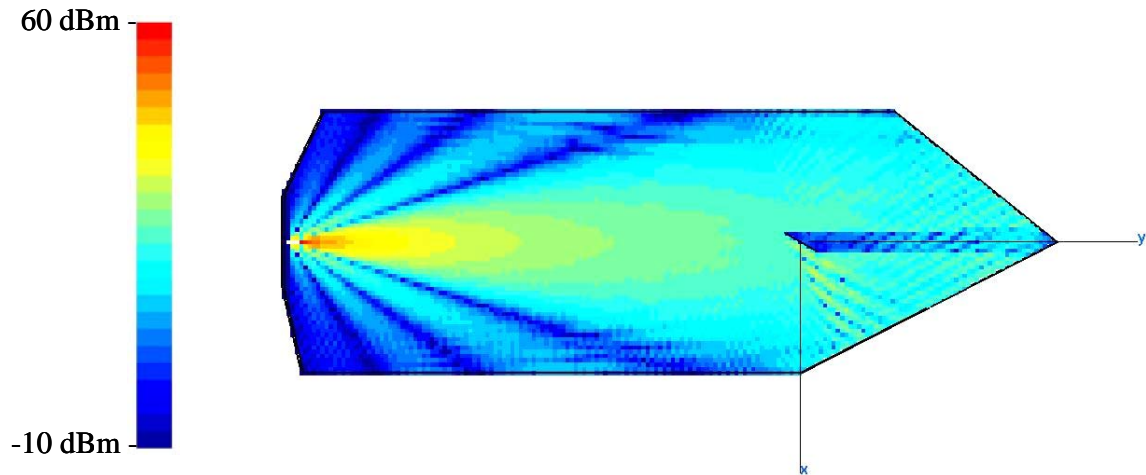


Figure 53. Vertically polarized 15 degree HPBW antenna with -27 dB absorber, no direct contribution and PEC plate with edge diffraction

For the case with no direct contribution, the reflections can be seen clearly. As expected, the reflected wave energy fades away quicker and the reflection contours appear to be weaker than for the -8.3 dB absorber case. The edge diffraction effects can be observed in Figure 55.

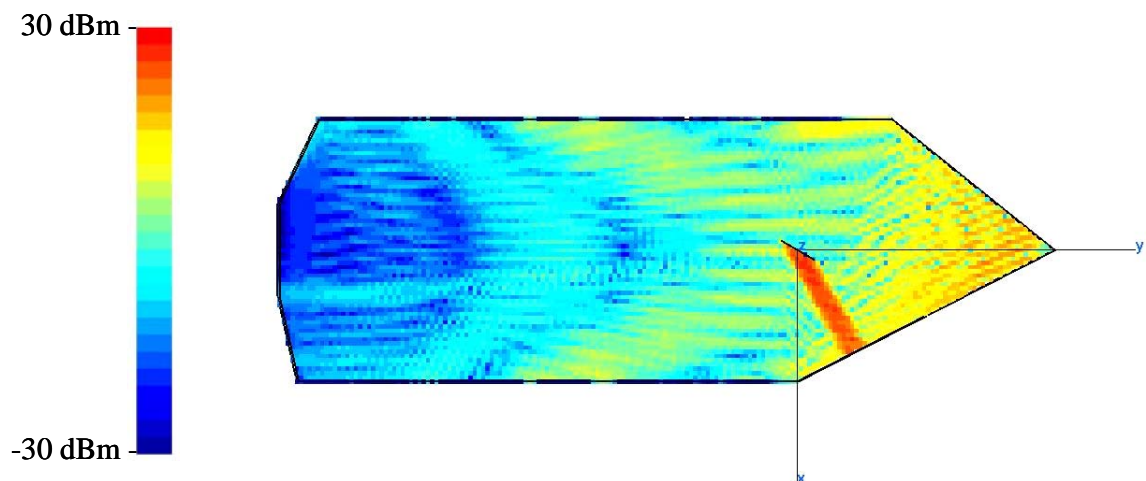


Figure 54. Vertically polarized 15 degree HPBW antenna with -27 dB absorber, no direct contribution with a PEC plate

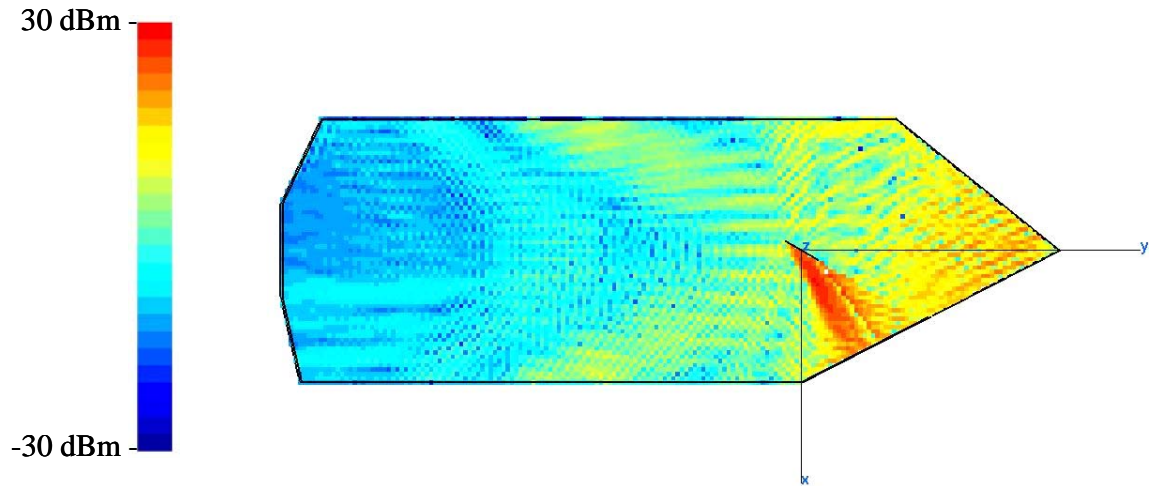


Figure 55. Vertically polarized 15 degree HPBW antenna with -27 dB absorber, no direct contribution with a PEC plate and edge diffraction included.

The same simulations are performed for a horizontally polarized antenna with the -27 dB absorber wall coating. The results are shown in Figures 56 through 59.

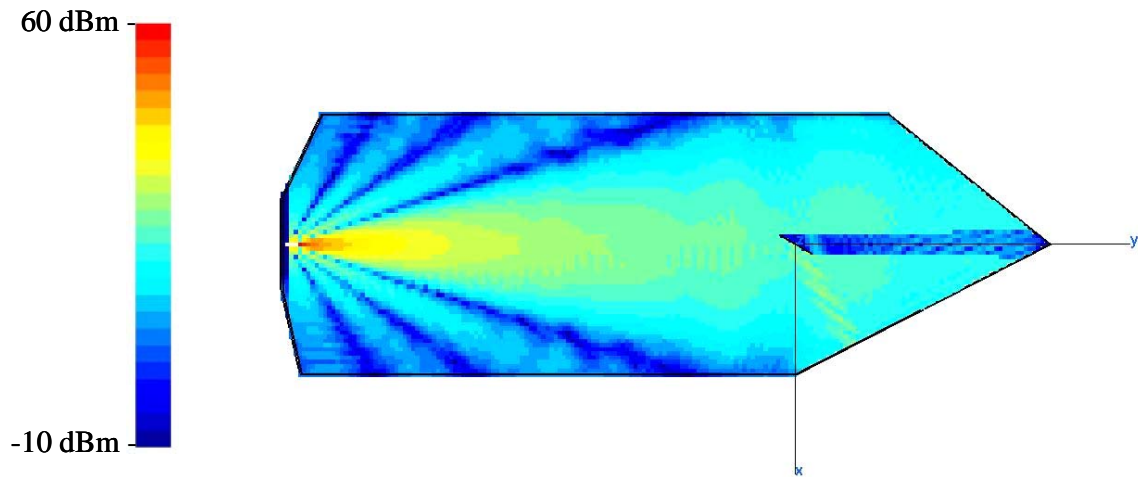


Figure 56. Horizontally polarized 15 degree HPBW antenna with -27 dB absorber, with a PEC plate, total field.

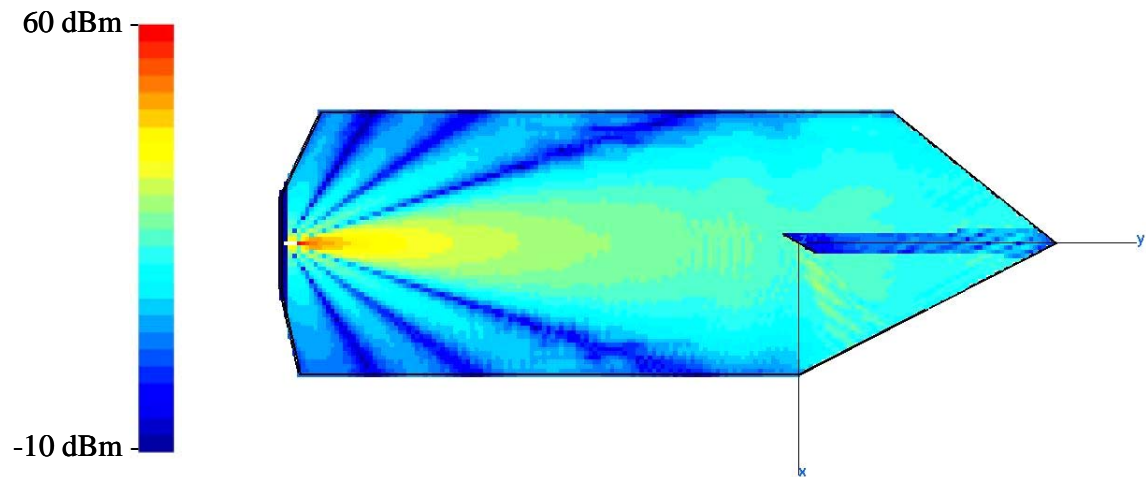


Figure 57. Horizontally polarized 15 degree HPBW antenna with -27 dB absorber, with a PEC plate and edge diffraction included, total field

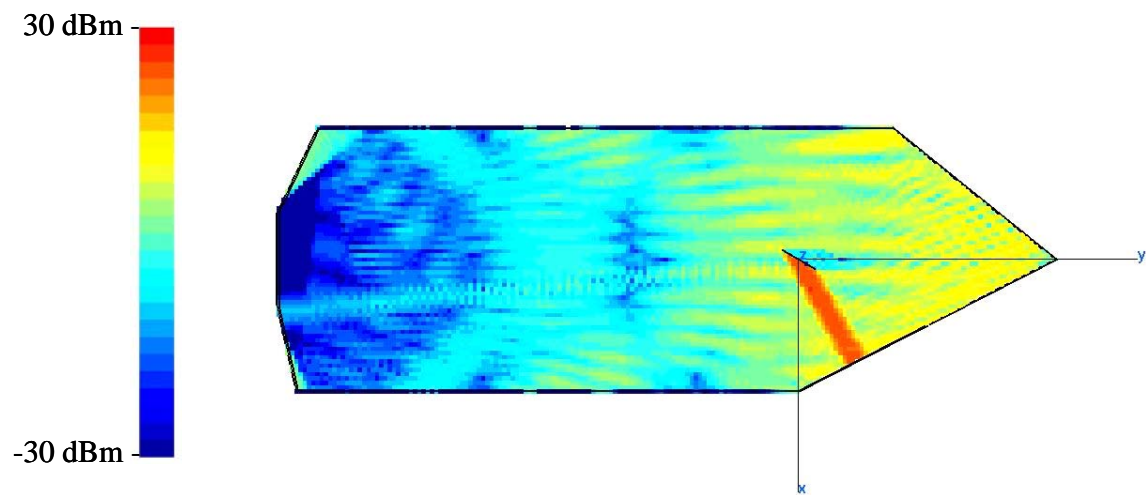


Figure 58. Horizontally polarized 15 degree HPBW antenna with -27 dB absorber, no direct contribution with a PEC plate

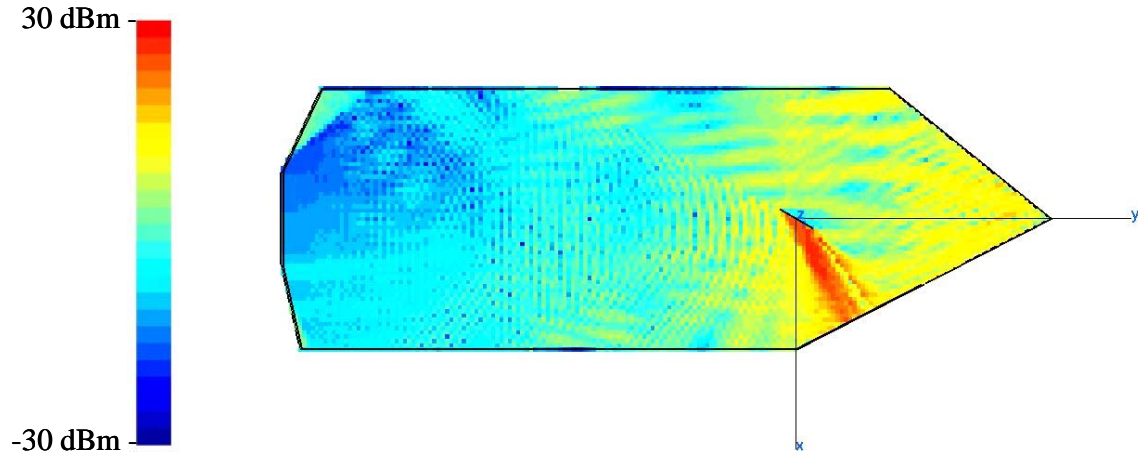


Figure 59. Horizontally polarized 15 degree HPBW antenna with -27 dB absorber, no direct contribution with a PEC plate and edge diffraction included.

2. Receiver Antenna in the Chamber

In order to see the transmitter antenna pattern and absorber effects, a vertically polarized circular aperture and 15 degree HPBW receiver antenna is placed at $(0,0,0)$. The receiver antenna was rotated with a step size of 2 degrees and the received power was recorded and plotted. The received power pattern compared with transmitted pattern is shown in Figure 60. The -8.3 dB absorber is used for the wall coatings.

The absorber effects can be seen in the figure from the sidelobe power levels. Since the pattern is normalized the peak value of the main beam is 0 dB. Ideally, the shape of the receive pattern is the same pattern as the transmitter pattern. The small differences are because of the chamber reflections and diffractions. Some of the steps in the receive pattern are due in part to quantization of the transmit pattern, which is defined in 4 degree increments. Urbana interpolates to obtain transmit gain values for other angles not in the pattern file.

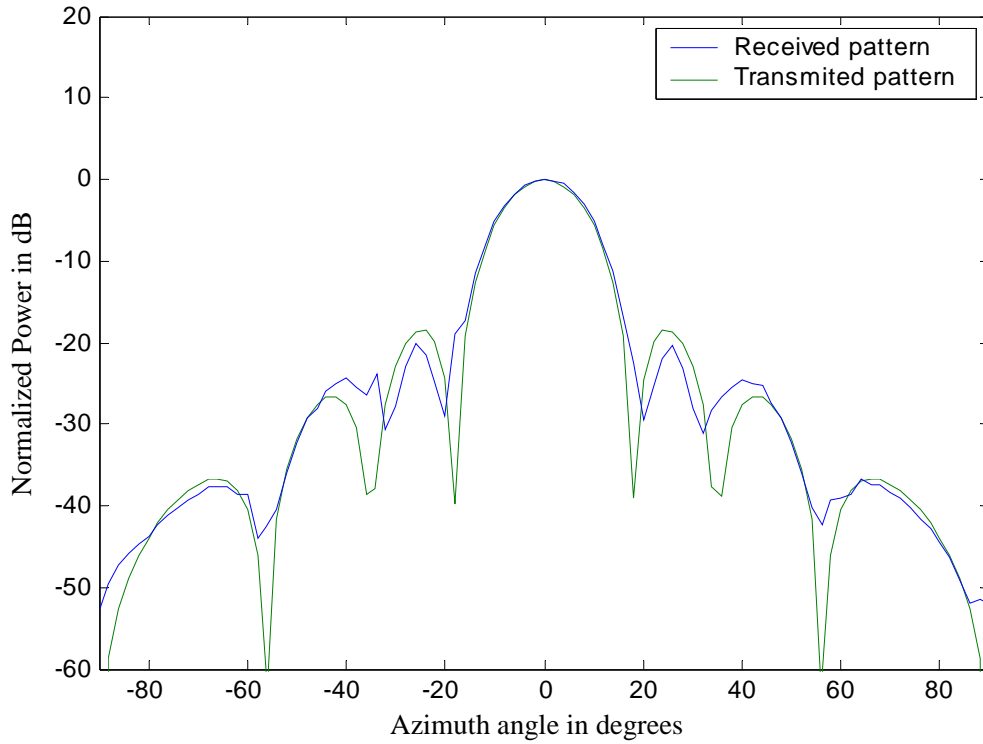


Figure 60. Receiver and transmitter antenna pattern comparison

F. SUMMARY

This chapter presented several simulations for the NPS anechoic chamber. A 2.0 GHz, 1W transmitting uniform circular aperture antenna was used throughout the simulations.

The beamwidths, polarization and the absorber types were changed and the propagation in the NPS anechoic chamber is observed by using the Urbana Wireless Toolset. In order to see the reflection edge diffraction effects a $L = 0.45$ m square plate is placed in the room. A receive antenna pattern was also simulated.

THIS PAGE INTENTIONALLY LEFT BLANK

V. SUMMARY AND CONCLUSIONS

A. SUMMARY

This thesis has examined the effectiveness of the Naval Postgraduate School (NPS) anechoic chamber for different types of absorbers for a circular aperture transmitting antenna at 2.0 GHz. It also included the measurement of ambient noise levels for the NPS anechoic chamber.

A series of simulations were performed for walls with perfect absorber, -8.3 dB reflection absorber and -27 dB reflection absorber by using the Urbana Wireless Toolset. The total field and reflected only cases for both vertical and horizontal polarizations were simulated. Different propagation mechanisms such as multiple reflections, diffraction and absorption effects have been observed in the NPS anechoic chamber. The HPBW of the antenna were varied from 15 degrees to 20 degrees. Typical values for the total fields were between -10 dBm and 60 dBm, and for the reflections only case it was in the range of -30 dBm and 30 dBm. The transmit power was 1 watt. The differences between the two absorbers were clearly visible for the reflected only case.

B. CONCLUSIONS

The results from the simulations indicated that the NPS anechoic chamber is not a good design for performing sensitive pattern measurements and making low noise and interference measurements. Although it is used for both research and instruction, it was actually built with only instruction in mind.

The pattern simulation for perfect absorber coatings was as expected. But, for the reflection only case with realistic absorber coatings, the quality of the pattern was not good, mainly due to multiple reflections from the walls in the wedge-shaped part of the chamber. This region behaves like a corner reflector and creates a hot spot in the chamber which corrupts any pattern measurement. The results were better for the -27 dB absorber

since it has a lower reflection coefficient. This shows that a more absorbent material would improve the NPS anechoic chamber.

The noise measurements for the anechoic chamber also show that it is not completely isolated from outside noise sources. They were taken in the range of 0-1000 MHz and the results were presented in Appendix B. The FM band noise can be seen from the measurement results. The best noise free performance is seen for the frequency range of 300-500 MHz.

C. FUTURE WORK

The thesis results can be used for redesigning the NPS anechoic chamber in the future in order to eliminate the existing problems. It also shows how the existing chamber configuration performs, so that current users can investigate any unexpected measured pattern data to see if it might be traced to the chamber characteristics.

Future work might include simulations with other absorber values. The chamber model can be refined further to include the pedestals (turntable), walkway, door seams and light fixtures. Different techniques for reducing the corner reflector effect at the wedge-shaped end of the chamber can also be investigated.

APPENDIX

A. URBANA INPUT FILE

The following is a sample Urbana input file that is used for the vertically polarized antenna pattern and perfect absorber coated walls.

```
--- input Urbana v 2.5
#
# *****
# A---scatterer file,length & freq
# *****
#--- name of scatterer file in ACAD format (e.g. wall.facet)
chamberconv.facet
#--- length unit:1=inch, 2=cm, 3=meter, 4=mm, 5=mil
1
#--- uniform freq (GHz): start freq, end , nstep
# (nstep=0 means: just do first freq. CAUTION: antenna patterns are
# assumed to be indep. of freq and is calculated at end freq)
2.0 2.0 0
#
# *****
# B--- Antenna Description and List
# *****
#
#---Enter method of describing antennas.
# (1 = here, 2 = file):
1
#---If described in file, enter file name:
dummy.txt
#---If described here, fill in sections B1, B2, B3.
# If described in file, use dummy data in sections B1, B2, B3
# (specify one dummy antenna type, dummy antenna origin,
# and one dummy item in antenna list).
#
# *****
# B1: Define Antenna Types
# *****
#
# Two lines for each type.
# Line1: type ID, ant code
# Line2: parameters
#
```

```

# Type ID must start from 1 and increment by 1 thereafter
#
# Ant Code  meaning      parameters
# -----  -
#   1      pattern file  filename(ascii)
#   2      dipole        length(real)
#
# Antenna Types list:
#
# Enter number of antenna types:
1
# Type #1
1 1
newpat15.txt
#
# *****
# B2: Enter origin of antenna coord in main coord
# *****
#
0. 0. 0.
#
# *****
# B3: Create Antenna List
# *****
#
# Three lines for each antenna.
# Line1: Type ID, location (x,y,z), power (watts), phase(deg)
# Line2: Local x-axis in main coord.
# Line3: Local z-axis in main coord.
#
# Enter number of antennas:
1
#
# Antenna #1
1 0. -242 58. 1. 0.
0. 0. 1.
0. 1. 0.
#
# *****
# C---Observation points
# *****
#--- Observation points defined with respect to main coord. system 7.
# Enter method of specifying list of points.
# (1 = here, 2 = file):
2

```

```

#--- If points are listed here, enter number of points (kobtot):
1
#--- If listed here (1 above), List xyz of points in main coord 7
# (one point at a line). If 2 above, include one dummy line.
1.      2.      -11.00
#--- If points listed in file (2 above), enter name of file.
observe.txt
#--- Include direct Tx to observer contribution.
# If you turn on the direct contribution from the transmitter to the
# observation point, computed result will be the total field, which is
# the incident + scattered field. For propagation analysis, this is
# the preferred setting. Otherwise, the result only includes the
# scattered field.
#
# Include direct contribution from transmitter to observation point (rx)
# (1 = yes, 0,2 = no):
1
#--- Compute received power into Rx antenna.
# Urbana always computes field levels at the observation point.
# If you specify an Rx antenna, Urbana will also compute the received
# power and record the results in the (runname).couple file.
# This causes a moderate but slow-down when using the SBR method (below).
#
# Include Rx antenna (1 = yes, 0,2 = no):
2
#--- Rx antenna specification
# Remaining entries in Section C can be ignored if not including
# an Rx antenna.
# Enter antenna type (1 = pattern file, 2 = dipole):
1
# Each antenna type requires additional parameters.
# List of expected parameters follows. Choose one.
#
# Type Description Expected Parameter(s)
# 1 Pattern File File Name (e.g., beam.antpat)
# 2 Dipole Length (in prevailing unit)
#
# Enter parameter(s) on next line:
dummy.antpat
#--- Rx antenna orientation
# Enter local x-axis of Rx in global coordinates
1. 0. 0.
# Enter local z-axis of Rx in global coordinates
0. 0. 1.
#

```

```

# *****
# D---Theoretical consideration
# *****
#--- Choose method of computation
# 0 = compute fields in the ABSENCE of the scatterer
# 1 = compute fields by SBR
# 2 = compute fields by GO
2
#--- If SBR, select a PO integration scheme at bounce points
# 1 = do integration at first & last bounce points only
# 2 = do so at all bounce points (GTD formulation)
2
#--- Edge diffraction
# SBR can be enhanced with PTD edge diffraction.
# GO can be enhanced with GTD edge diffraction.
# Add edge diffraction (0,2=no, 1=ILDC (SBR or GO), 3=UTD (GO only)
2
#--- If edge diffraction switched on, enter name of edge file
# (e.g., wall.edge or dummy if edge not included).
dummy.edge
#--- Choose method of ray launch
# 1 = by (baby) facet, achieving a uniform first bounce surface density
# 2 = uniform angular distribution (burst launch)
# (If computation by GO, must select 2 = burst launch)
2
#--- If ray launch by (baby) facet (1 above), enter ray density:
# # rays/wavelength (normally 5-10)
5.
#--- If burst ray launch (2 above), enter angular interval (deg).
# (Typically 0.25 - 2.0 deg)
1
#--- max permissible ray bounces (normally 5-10)
5
#--- max-voxdepth = max depth of BSP tree (normally 20)
# max-voxl = max facets in each voxel (normally 10)
# (Larger voxdepth & smaller voxl lead to faster ray tracing
# but more computer memory)
15,10
#--- ICOAT for absorbing facets
1
#--- IQMATRIX for divergence factor
# 1 = calculated by Q-matrix
# 2 = ignored except for the spherical wave spread
2
#--- IF using Q-matrix, name target curvature file(e.g. wall.curv)

```



```

# -----
# ADVANCE1: ADD GTD-TYPE BLOCKAGE CHECK
# -----
# In regular urbana computation, blockage check is mostly done by
# PTD principle. For interior scattering in a confined region, use of
# GTD principle may be more appropriate.
# Option to use GTD principle: 1=yes, 2=no (regular case)
2
# -----
# ADVANCE2: SIMPLE TERRAIN BLOCKAGE MODEL
# -----
# For GO method, terrain generates 100% blockage, and blocked rays leave
# no energy behind a hill. With this feature, LOS rays and UTD edge
# diffraction rays can pass through terrain, with some attenuation.
# Attenuation is measured in dB per hill. Each hill is identified
# by two passages through two terrain facets.
# Can only be used with GO method (and UTD edge option).
# Use simple terrain model: 1 = yes, 2 = no (regular case)
2
# Enter coating code range of terrain facets (e.g., 1, 2):
1 1
# Enter amount of attenuation per hill (dB, > 0):
5.
# -----
# ADVANCE3: APPROXIMATE DOUBLE DIFFRACTION MODEL
# -----
# For GO + UTD method, only single diffraction is considered.
# With this feature, double diffraction is approximated by identifying
# surfaces which block the single diffraction, such as building walls.
# If one or two facets block the path from the single diffraction point
# to the transmitter, the diffraction is still included, but with attenuation.
# Works best if "diffracting facets", marked by their coating code, are
# always associated with enclosed structures with well defined edges.
# Use double diffraction model: 1 = yes, 2 = no (regular case)
2
# Encounter coating code range of diffracting facets (e.g., 5, 10):
2 2
# Enter amount of attenuation for second diffraction (dB, > 0);
10.
# -----
# ADVANCE4: ACCELERATION
# -----
# For large scenes, run time grows both with the number of field
# observation points and the number of edges. Normally, all combinations
# of lit edges and observation points are considered. This feature

```

```

# accelerates the processing by limiting the scope of considered edge
# interactions to region around the LOS path from the transmitter
# to the observation point. For example, to run a 5 km by 5 km scene,
# one may choose a 250 m interaction radius. For each observation
# point, edges are ignored that lie outside an ellipse whose foci are the
# Tx and the observation point and whose major axis is the LOS distance
# plus 500 m (radius x 2).
# This feature can also be used to automatically filter edge files
# whose domain far exceeds the domain of observation points.
# Only use this feature for terrestrial simulations where the scene
# is nominally parallel to the x-y plane.
#
# Use large scene acceleration: 1 = yes, 2 = no (regular case)
2
# Enter radius of interaction
250.
# -----
# ADVANCE5: MULTI-DIFFRACTION
# -----
# Substitute for Adv. #3. Uses ray rubber-banding algorithm to find
# path from transmitter to receiver.
# Can only be used with GO. Cannot be used in conjunction with Adv. #3.
# If UTD switched on above, will take measures not to double count
# single diffraction mechanisms.
# Use multi-diffraction model: 1 = yes, 0,2 = no
2
# Enter coating code range of diffracting facets (e.g. 5, 10):
2 2
# Enter maximum number of rubber-band points ( also used in Advance6 )
1
# Check multiple crawl planes instead of just vertical one: 1 = yes, 0,2 = no
0
# -----
# ADVANCE6: REFLECTION-DIFFRACTION
# -----
# If UTD switched on above, will take measures not to double count
# single diffraction mechanisms.
# Use reflection-diffraction model: 1 = yes, 0,2 = no
2
# Do more than just single diffractions: 1 = yes, 0,2 = no
# Allow rubber-banding to both transmitter and receiver: 1 = yes, 0,2 = no
1 0
# Choose crawl plane selection mode: 0 = always vertical, 1 = initial edge,
# 2 = adaptive from edge to edge
1

```



```
# -----  
# ADVANCE7: GREEN'S FUNCTION (GF) FILE  
# -----  
# By default, for SBR and no-target methods, a GF file IS NOT produced.  
# Also, by default, for GO, a GF file IS produced.  
# Use this feature to explicitly activate or de-activate generation  
# of the GF file, which is needed by the re-processor for its activities.  
# Activate GF file: 0 = no, 1 = yes, 2 = default activation behavior  
2  
# If yes, enter buffer scale factor. Increasing scale factor reduces  
# the number of GF file dumps to disk during a run, but costs memory.  
# Recommend 2 - 5 for GO method, 1 for no-target method,  
# and 100 - 10000 for SBR method.  
2
```

B. ANECHOIC CHAMBER MEASUREMENTS

The following figures present the noise measurements performed by Naval Postgraduate School laboratory staff for the NPS anechoic chamber. These measurements were taken for the frequency ranges of 0-1000 MHz with a step size of 100 MHz. These measurements show that the NPS chamber provides little isolation from external signal sources.

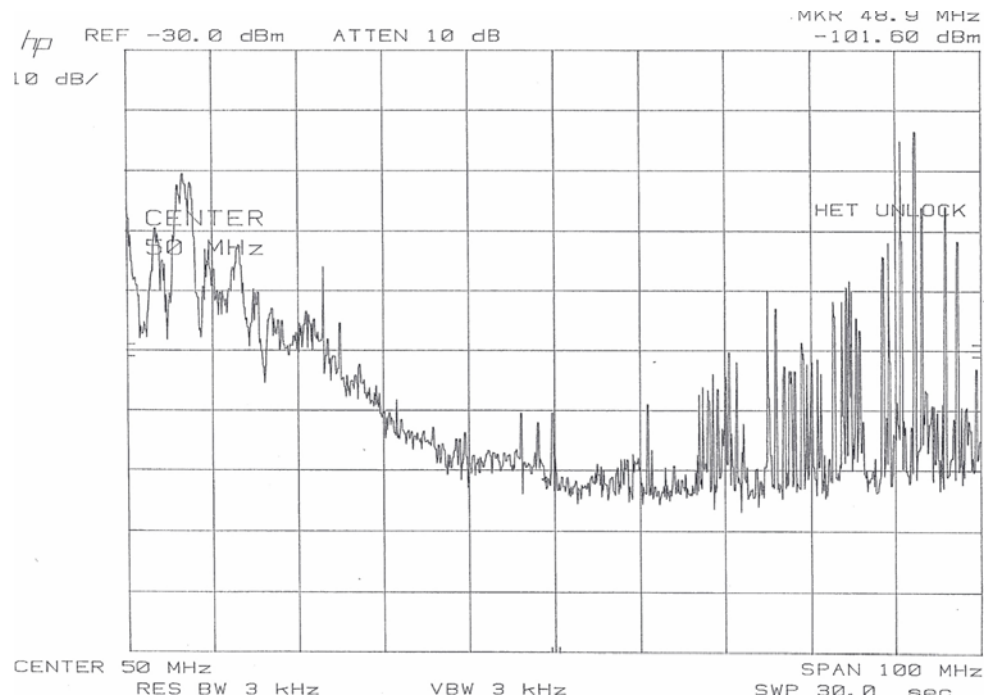


Figure 61. The noise measurement in 0-100 MHz frequency range for the Naval Postgraduate School anechoic chamber

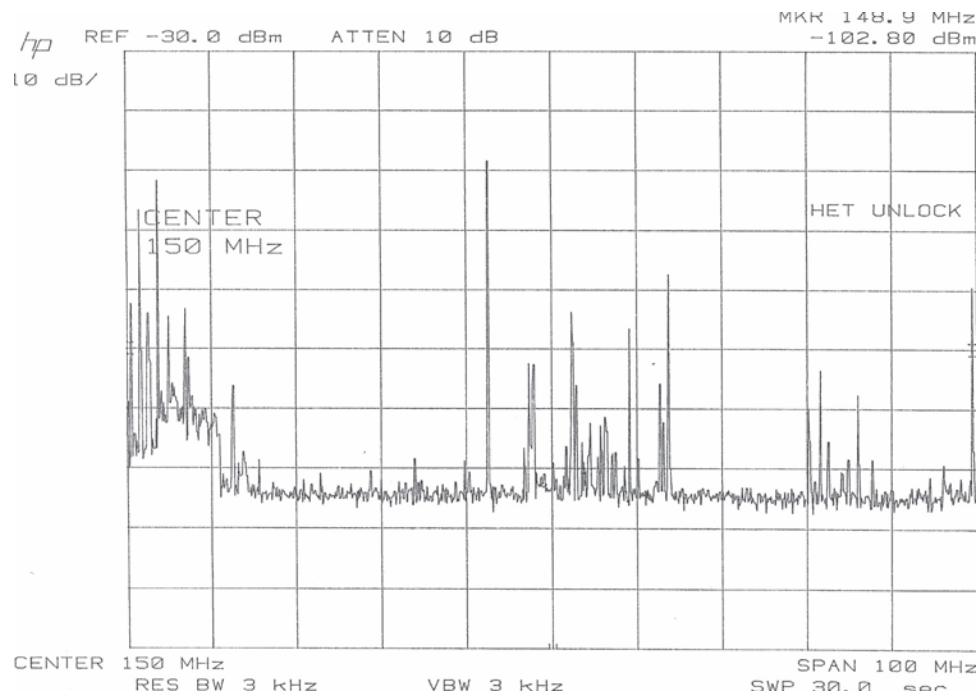


Figure 62. The noise measurement in 100-200 MHz frequency range for the Naval Postgraduate School anechoic chamber

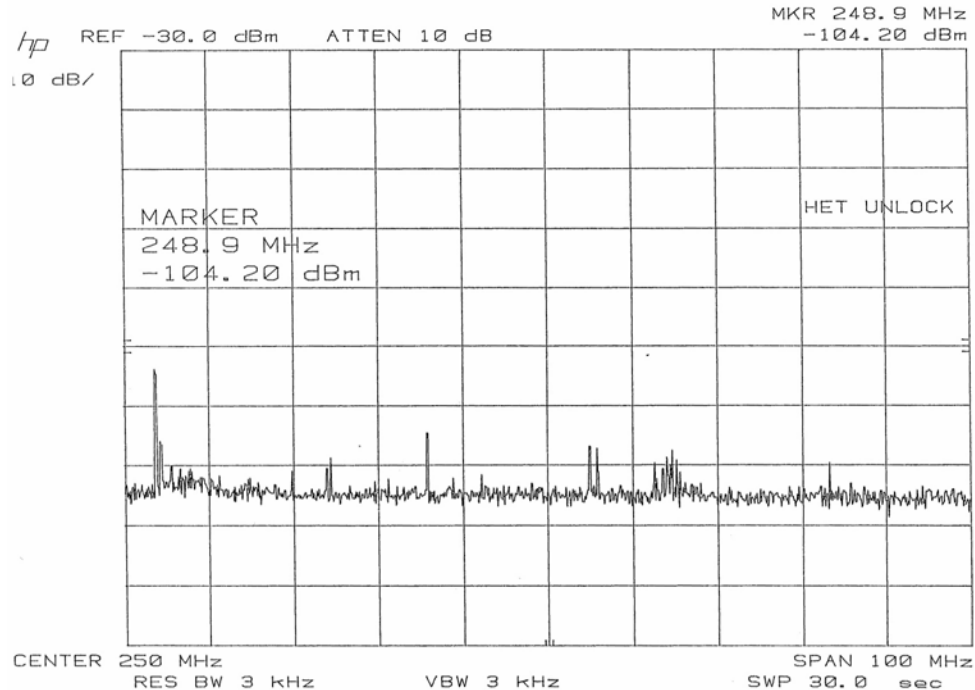


Figure 63. The noise measurement in 200-300 MHz frequency range for the Naval Postgraduate School anechoic chamber

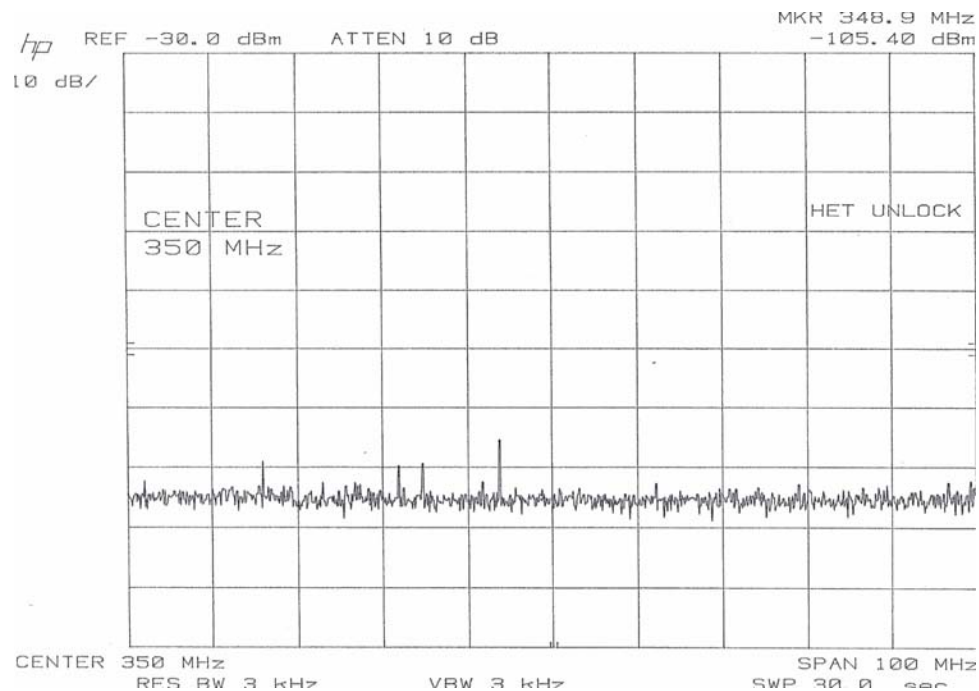


Figure 64. The noise measurement in 300-400 MHz frequency range for the Naval Postgraduate School anechoic chamber

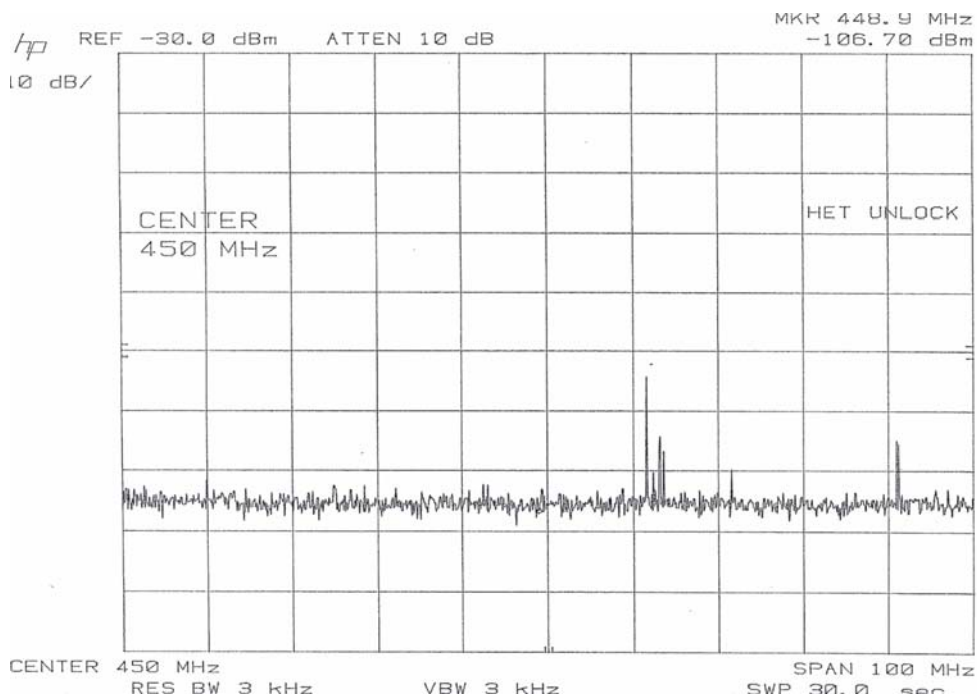


Figure 65. The noise measurement in 400-500 MHz frequency range for the Naval Postgraduate School anechoic chamber

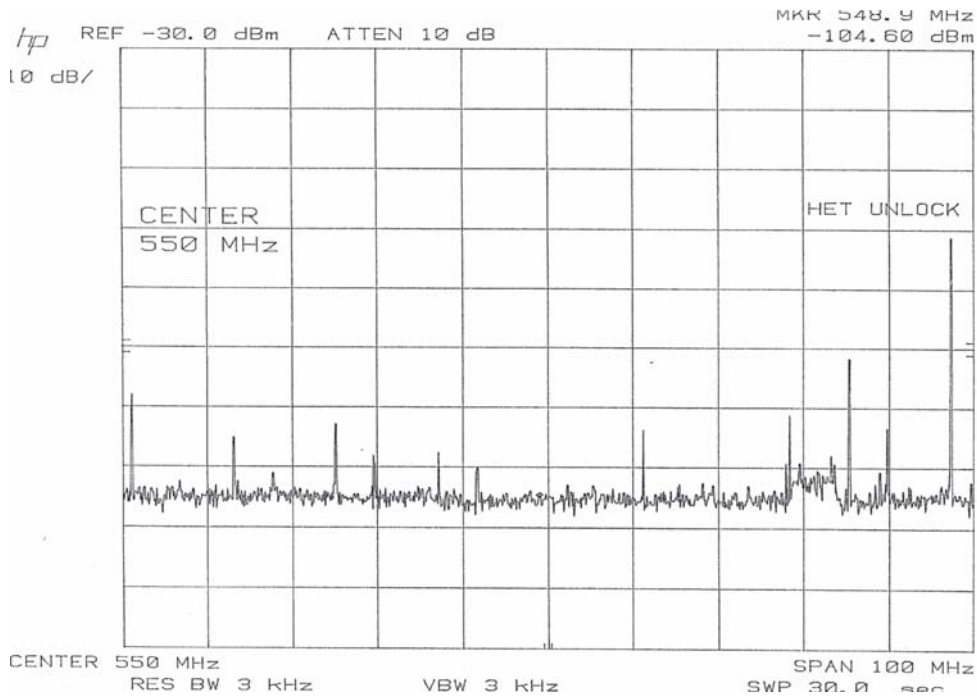


Figure 66. The noise measurement in 500-600 MHz frequency range for the Naval Postgraduate School anechoic chamber

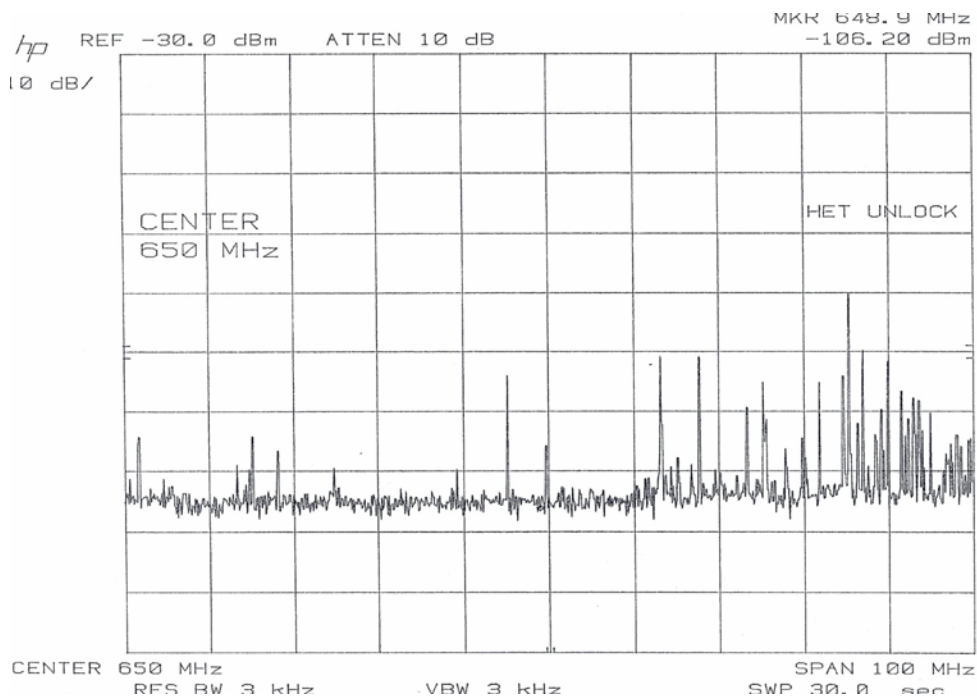


Figure 67. The noise measurement in 600-700 MHz frequency range for the Naval Postgraduate School anechoic chamber

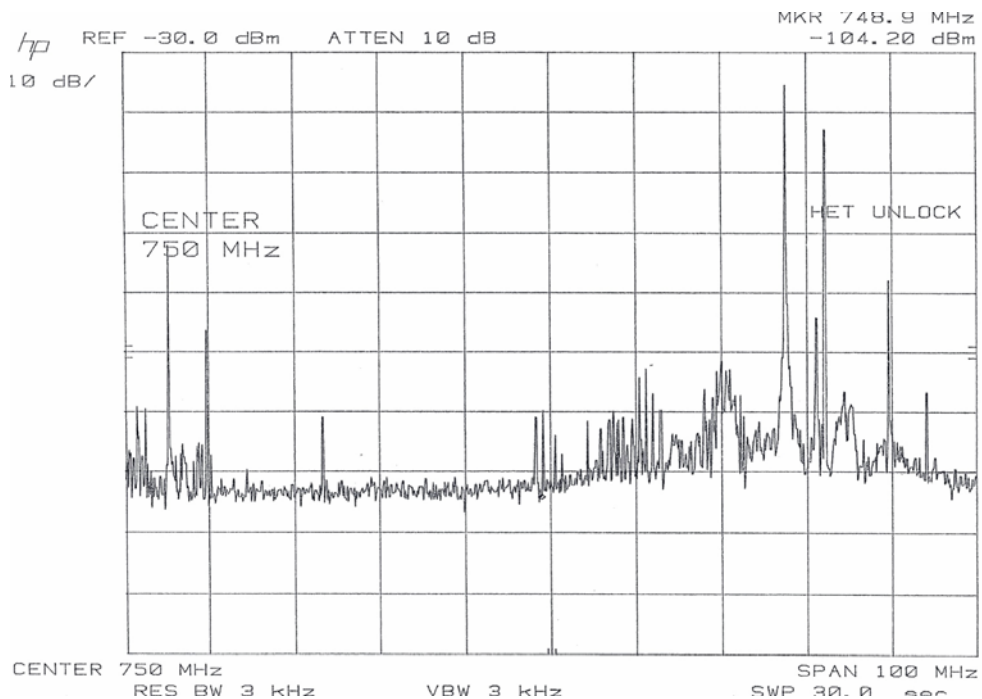


Figure 68. The noise measurement in 700-800 MHz frequency range for the Naval Postgraduate School anechoic chamber

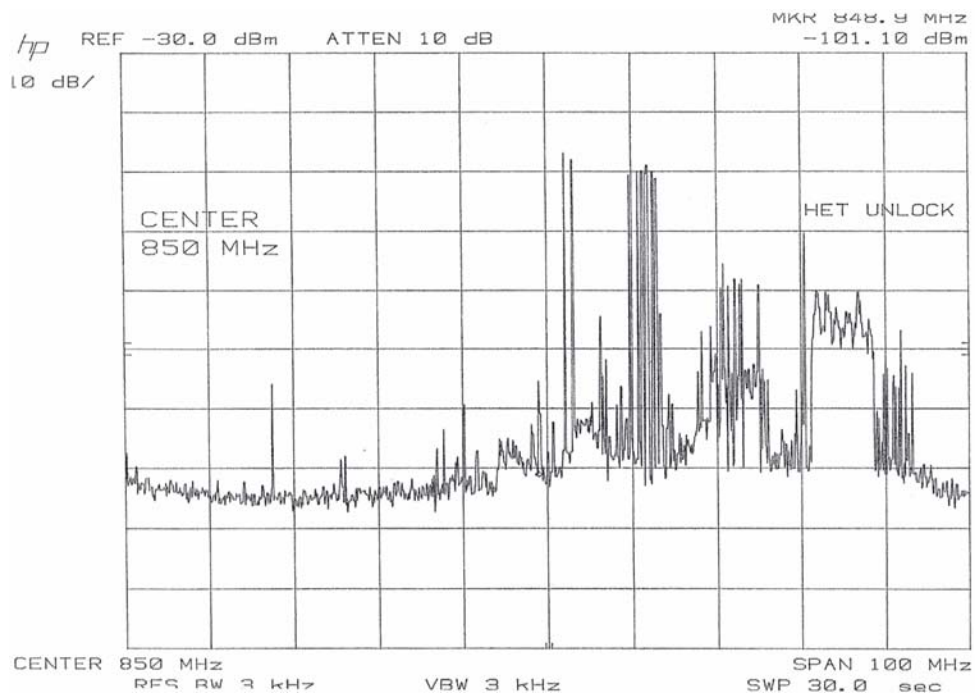


Figure 69. The noise measurement in 800-900 MHz frequency range for the Naval Postgraduate School anechoic chamber

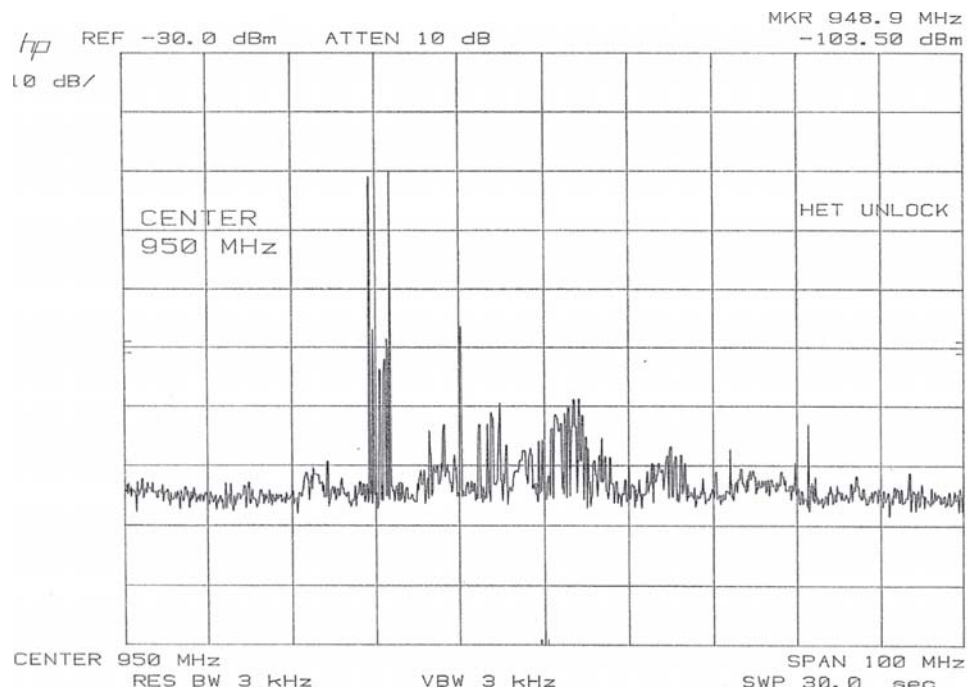


Figure 70. The noise measurement in 900-1000 MHz frequency range for the Naval Postgraduate School anechoic chamber

C. MATLAB CODES

The following is a list of MATLAB codes which includes the radar absorbing material design, the antenna pattern, the observation points generation, and the amplitude error and phase error calculations.

```
%Radar Absorbing Material Design
%-----
clear;
clc;
f=input('Input Frequency in Ghz= ');
t=input('Enter thickness in inches= ');
f=f*1e9;t=t*0.0254;
lambda=(3*1e8)/f;
Bo=2*pi/lambda;
Er=4;
Mr=1;Mrr=0;
v=1;
Mo=4*pi*1e-7;
E0=8.85e-12;
Zo=377;

for Err=0:0.5:20
    gamma(v)=j.*Bo.*(((Mr-j.*Mrr).*(Er-j.*Err)).^0.5);
    zd(v)=((Mo.*(Mr-j.*Mrr))./(E0.*(Er-j.*Err))).^0.5;
    v=v+1;
end

zin=zd.*tanh(gamma*t);
ref=((zin-Zo)./(zin+Zo));
refdb=20.*log10(abs(ref));
Err=0:0.5:20;

plot(Err,refdb);
title('Material Thickness= 2.24 inches');
ylabel('Reflection Coefficient');
xlabel('Permeability-Epsilon double prime');
grid on;
```



```

% Antenna pattern file generation for Urbana
%-----
clc;
clear;
c=3*10^8;
lamda =c/(2.0*10^9);
HPBW = 15;
a = 58.4 * lamda / (2*HPBW);
beta = 2*pi/lamda;
E0 = 1;
E = j*beta*E0*pi*a^2/(2*pi);

Directivity = (4*pi*pi*a^2)/lamda^2
Directivity_dB = 10*log10(Directivity)

step1 = 90; % Vertical Steps
step2 = 180; % Horizontal Steps
d_theta = 180/(step1);
d_phi = 360/(step2);
k = 0;
ip = 0;
iq = 0;

for phi = 0:d_phi:360
    for theta = 0.01:d_theta:180.01
        k = k+1;
        f = 2*besselj(1,beta*a*sin(theta*pi/180))/(beta*a*sin(theta*pi/180));
        e_theta = cos(phi*pi/180)*E*f;
        e_phi = -sin(phi*pi/180)*cos(theta*pi/180)*E*f;
        if theta > 90
            e_theta = 0;
            e_phi = 0;
        end
        if phi == 0
            ip = ip + 1;
            et0(ip) = 20*log10(abs(e_theta));
            ep0(ip) = 20*log10(abs(e_phi));
            eth(ip) = theta;
        end
        if phi == 90
            iq = iq + 1;
            et90(iq) = 20*log10(abs(e_theta));
            ep90(iq) = 20*log10(abs(e_phi));
            eth90(iq) = theta;
        end
    end
end

```

```

        A(k,1:4) = [real(e_theta), imag(e_theta), real(e_phi), imag(e_phi)];
    end
end
save newpat15 A -ASCII;

```

```

% Observation Points generation

```

```

%-----

```

```

clc;
clear;
x=-80:2:80;
y=-260:2:140;
z=5;
v=1;
for i=1:201;
for k=1:81;
    pts(v,1)=x(k);
    pts(v,2)=y(i);
    pts(v,3)=z;
    v=v+1;
end
end
save observe pts -ASCII;

```

```

% Amplitude Error

```

```

%-----

```

```

clear;
clc;
lambda=0.15;
k=4*log(2);
R=242*0.0254;
Pt=1;
Pr0=Pt*1/(4*pi*R^2);

for tetab=5:5:20; % half power angle (HPBW/2)
    disp(['HPBW =', num2str(2*tetab)])
    i=0;
    tetac=tetab*(pi/180);
    for L=0.02:0.02:1.5;
        i=i+1;
        teta=atan(L/(2*R));
        T(i)=teta*180/pi;
        Pt=1;
        g(i)=exp(-k*teta^2/(tetac/2)^2);
    end
end

```

```

Pr=Pt*g(i)/(4*pi*R^2*Pr0);
Prdb(i)=10*log10(Pr);
%pherr(i)=pi.*L.^2/(4*R*lambda);
LL(i)=L;
end

```

```

plot(LL,Prdb);
xlabel('Length of L in meters');
ylabel('Amplitude error in dB');
grid on;
%clear g,Prdb,pherr;
hold on
end
axis([0,max(LL),-5,0])
gtext('5 degree HPBW');
gtext('10 degree HPBW');
gtext('15 degree HPBW');
gtext('20 degree HPBW');
hold off

```

```

%Phase Error
%-----
clc;
clear;
lambda=0.15;
k=4*log(2);
R=242*0.0254;
i=0;
for L=0.01:0.01:1.5;
    i=i+1;
    D=sqrt(R^2+(L/2)^2);
    del=D-R;
    pherr(i)=2*pi*del/lambda;
    phdeg(i)=pherr(i)*180/pi;
    LL(i)=L;
end
plot(LL,phdeg);
xlabel('Length of L in meters');
ylabel('Phase error in degrees');
grid;

```

LIST OF REFERENCES

1. www.eccosorb.com, July 2004.
2. David C. Jenn, *Radar and Laser Cross Section Engineering*, AIAA, 1995.
3. David C. Jenn, Lecture notes for EC 3630, Radio Wave Propagation, available at www.nps.navy.mil/jenn, 2003.
4. Fahwaz T. Ulaby, *Fundamentals of Applied Electromagnetics*, Media Edition, Prentice Hall, 2001.
5. Asoke K. Bhattacharyya and D.L Sengupta, *Radar Cross Section Analysis & Control*, Artech House, 1991.
6. www.westhamptonbeach.k12.ny.us/.../energy.htm, July 2004.
7. R. Reed and C. M. Russel, *Ultra High Frequency Propagation*, John Wiley and Sons, 1953.
8. O. Landron, M. J. Feuerstein, and T. S. Rappaport, "In site microwave reflection coefficient measurements for smooth and rough exterior wall surfaces," *Proceedings IEEE Vehicular Technology Conference*, pp. 77.80, May 18.20, 1993.
9. <http://www.saic.com/products/software/urbana/>, July 2004.
10. Eugene F. Knott, John F. Shaeffer and Michael T. Tuley, *Radar Cross Section*, Second edition, Artech House, 1993.
11. http://www.comtest.nl/em/anechoic_chambersem.htm, July 2004.
12. <http://www.conformity.com/0201spotlight.pdf>, July 2004.
13. Warren L. Stutzman and Gary A. Thiele, *Antenna Theory and Design*, John Wiley & Sons, New York, 1999.

THIS PAGE INTENTIONALLY LEFT BLANK

INITIAL DISTRIBUTION LIST

1. Defense Technical Information Center
Ft. Belvoir, Virginia
2. Dudley Knox Library
Naval Postgraduate School
Monterey, California
3. Chairman
Information Sciences Department
Monterey, CA
4. Professor David C. Jenn
Department of Electrical and Computer Engineering
Monterey, CA
5. Professor Curtis Schleher
Department of Information Science
Monterey, CA
6. Professor Jeffrey B. Knorr
Department of Electrical and Computer Engineering
Monterey, CA
7. Professor Richard W. Adler
Department of Electrical and Computer Engineering
Monterey, CA
8. Professor Jovan Lebaric
Department of Electrical and Computer Engineering
Monterey, CA
9. LTJG Burcak Erenoglu
Turkish Navy
Ankara, TURKEY